Electronic Supplementary Material (ESI) for Chemical Communications.

Role of Symmetry Breaking in the Structural Trapping of Light-Induced Excited Spin States

Rafal Kulmaczewski,[a] Elzbieta Trzop,[b] Laurence J. Kershaw Cook,[c] Eric Collet,[b,*] Guillaume Chastanet[d,*] and Malcolm A. Halcrow[a,*]

[a] *School of Chemistry, University of Leeds, Woodhouse Lane, Leeds LS2 9JT, United Kingdom.*
E-mail: m.a.halcrow@leeds.ac.uk

[b] *Institut de Physique de Rennes, Université de Rennes 1, UMR UR1-CNRS 6251, 35000 Rennes (France)*
E-mail: eric.collet@univ-rennes1.fr

[c] *Department of Chemistry, University of Bath, Claverton Down, Bath BA2 7AY, UK*

[d] *CNRS, Université de Bordeaux, ICMCB, UPR 9048, F-33600 Pessac, France.*
Email: chastanet@icmcb-bordeaux.cnrs.fr

Supporting Information

Synthesis and Characterisation of $\mathbf{1[ClO_4]_2}$·solv Page

Photomagnetic and Photocrystallographic Data from $\mathbf{1[BF_4]_2}$·solv and $\mathbf{1[ClO_4]_2}$·solv Page

Synthesis and Characterisation of $1[ClO_4]_2 \cdot solv$

Experimental

Instrumentation

The magnetic susceptibility measurements in Figure S5 were performed with freshly isolated, unground polycrystalline samples, using a Quantum Design SQUID/VSM magnetometer in an applied field of 5000 G and a temperature ramp of 5 $Kmin^{-1}$. Diamagnetic corrections for the samples were estimated from Pascal's constants;[1] a previously measured diamagnetic correction for the sample holder was also applied to the data. It was not possible to use the same material for both measurments, because the in situ annealing experiments performed inside the magnetometer led to partial desolvation of the materials.

Elemental microanalyses were performed by the University of Leeds School of Chemistry microanalytical service, or the London Metropolitan University School of Human Sciences microanalytical service. Electrospray mass spectra (ESMS) were obtained on a Bruker MicroTOF spectrometer, from MeCN feed solutions. All mass peaks have the correct isotopic distributions for the proposed assignments. X-ray powder diffraction measurements were obtained from a Bruker D2 Phaser diffractometer, using Cu-K_α radiation (λ = 1.5419 Å).

Materials and methods

4-(*Iso*propylsulfanyl)-2,6-di(pyrazol-1-yl)pyridine (*L*) and all the **1[BF$_4$]$_2$**·solv materials were prepared as previously described.[2] Other reagents and solvents were purchased commercially and used as supplied. All reactions were carried out in air using as-supplied AR-grade solvents.

Synthesis of [Fe(*L*)$_2$][ClO$_4$]$_2$ (1[ClO$_4$]$_2$). Solid *L* (76 mg, 0.28 mmol) was added to a suspension of $Fe[ClO_4]_2.6H_2O$ (37 mg, 0.11 mmol) in nitromethane (15 cm^3), causing the solution to become an intense yellow color. After stirring for 30 mins, the orange-yellow solution was filtered. Diethyl ether (100 cm^3) was added slowly over 10 minutes and the resulting yellow solid was collected on a glass frit and washed with additional Et_2O. Yield 74 mg, 84 %.

Crystalline samples of **1[ClO$_4$]$_2$**·$MeNO_2$, **1[ClO$_4$]$_2$**·MeCN and **1[ClO$_4$]$_2$**·*y*Me_2CO were grown by slow diffusion of diethyl ether vapour into solutions of the complex in those solvents. The hydrate **1[ClO$_4$]$_2$**·H_2O was prepared by drying **1[ClO$_4$]$_2$**·*y*Me_2CO *in vacuo* for 24 hrs at room temperature, then exposing it to air.

Elemental analysis for **1[ClO$_4$]$_2$**·$MeNO_2$. Found: C, 39.7; H, 3.70; N, 17.3 %. Calcd for $C_{28}H_{30}Cl_2FeN_{10}O_8S_2{\cdot}CH_3NO_2$: C, 39.3; H, 3.75; N, 17.4 %.

Elemental analysis for **1[ClO$_4$]$_2$**·MeCN. Found: C, 41.8; H, 3.70; N, 17.9 %. Calcd for $C_{28}H_{30}Cl_2FeN_{10}O_8S_2{\cdot}CH_3CN$: C, 41.6; H, 3.84; N, 17.8 %.

Elemental analysis for **1[ClO$_4$]$_2$**·*y*Me_2CO (*y* = 0.7). Found: C, 42.2; H, 4.00; N, 16.2 %. Calcd for $C_{28}H_{30}Cl_2FeN_{10}O_8S_2{\cdot}0.7(CH_3)_2CO$: C, 41.8; H, 4.00; N, 16.1 %.

Elemental analysis for **1[ClO$_4$]$_2$**·H_2O. Found: C, 39.7; H, 3.70; N, 17.0 %. Calcd for $C_{28}H_{30}Cl_2FeN_{10}O_8S_2{\cdot}H_2O$: C, 39.9; H, 3.82; N, 16.6 %.

WARNING Although we encountered no issues in handling 1[ClO$_4$]$_2$ during this study, metal/organic perchlorates are potentially explosive and should be handled with care in small quantities. TGA analyses of the 1[ClO$_4$]$_2$·solv samples were not obtained for that reason.

Single crystal X-ray structure determinations of 1[ClO$_4$]$_2$·solv

Crystals of **1[ClO$_4$]$_2$**·$MeNO_2$, **1[ClO$_4$]$_2$**·MeCN, **1[ClO$_4$]$_2$**·*y*Me_2CO and **1[ClO$_4$]$_2$**·H_2O were prepared as described above, while the crystal of **1[ClO$_4$]$_2$**·sf was generated by heating a crystal of **1·H$_2$O** at 375 K on the diffractometer for 30 mins. A *SQUEEZE* analysis[3] from the final refinements of that **1[ClO$_4$]$_2$**·sf crystal implied that its solvent-accessible void space contains 4 and 7 unresolved electrons per unit cell, corresponding to 0.10 and 0.18 equiv of residual H_2O respectively (10 electrons per molecule). The same crystal of each compound was used for structure determinations at multiple temperatures and, where relevant, for the variable temperature unit cell data in Fig. S4.

All diffraction data were collected with an Agilent Supernova dual-source diffractometer, using monochromated Cu-K_α radiation (λ = 1.54184 Å). The diffractometer is fitted with an Oxford Cryosystems low-temperature device. Experimental details of the structure determinations are given in Table S1. The structures were solved by direct methods (*SHELXS97*[4]), and developed by full least-squares refinement on F^2 (*SHELXL97*[4]). Crystallographic figures were prepared using *X-SEED*.[5]

Structure refinement details for 1[ClO_4]$_2$·solv
Unless otherwise stated, the following procedures were used to model disordered residues. For disordered *iso*propylsulfanyl groups, fixed restraints were applied: C(pyridyl)–S = 1.75(2), C(alkyl)–S = 1.82(2), C–C = 1.52(2), 1,3-C–C–C = 2.48(2) and 1,3-C–S–C = 2.83(2) Å. In contrast, refined B–F or Cl–O, and F…F or O…O, distance restraints were applied to disordered anions. Unless otherwise stated all non-H atoms with occupancy >0.5 were refined anisotropically, and H atoms were placed in calculated positions and refined using a riding model.

Structure refinements of 1[ClO_4]$_2$·$MeNO_2$. At 250 K, one of the isopropyl substituents on the complex cation is disordered over two equally occupied orientations, which modelled successfuly without restraints. Both ClO_4^- ions are also disordered, one over two half-occupied sites and the other over three equally occupied orientations. Finally, the nitromethane molecule is also disordered and was refined with three sites with occupancies of 0.50, 0.35 and 0.15. These were modelled with the fixed restraints C–N = 1.45(2), N–O = 1.22(2), O...O = 2.09(2) and C...O = 2.32(2) Å. The nitromethane molecule and one perchlorate ion were still disordered at 147 and 100 K, which were refined using the same procedures with slightly different occupancy patterns at the two temperatures. CCDC 1428759-1428760, 1563026

Structure refinements of 1[ClO_4]$_2$·MeCN. In the high temperature structure, one isopropyl substitutent is disordered over two equally occupied orientations, which were modelled with fixed distance restraints. Both anions are also disordered, one over two sites and the other over three sites. Finally, the acetonitrile molecule is also disordered across three sites with occupancies of 0.40, 0.40 and 0.20. These were modelled with the fixed restraints C–C = 1.48(2), C–N = 1.15(2) and 1,3-C–C–N = 2.63(2) Å. None of this disorder was evident in the same structure at 142 K. CCDC 1428761-1428762

Structure refinements of 1[ClO_4]$_2$·*y*Me_2CO (*y* ≈ 0.70). At 250 K, one isopropyl substituent is disordered over three equally occupied orientations, two of which share a common S atom. These were modelled as above. Both ClO_4^- ions are also disordered, over two and three equally occupied orientations. Finally, the acetone solvent molecule is also badly disordered. Three partial solvent sites were located in the Fourier map, which were each refined with 0.25-occupancy. The fixed restraints C–O = 1.22(2), C–C = 1.51(2), 1,3-C...C = 2.62(2) and 1,3-C...O = 2.37(2) Å were applied to these sites. An anti-bumping restraint was also required in this structure between H(15) and the symmetry-related solvent methyl group C(54^{vi}) (symmetry code: (vi) 1−*x*, 1−*y*, 1−*z*). All fully occupied non-H atoms, plus the two-thirds occupied S atom, were refined anisotropically. Apart from one perchlorate ion which had become ordered, the same disorder was still present in the 147 K structure and was modelled in the same way. CCDC 1428763-1428764

Structure refinements of 1[ClO_4]$_2$·H_2O. At In the 250 K structure, one of the isopropylsulfanyl substitutents on the complex cation is disordered over three orientations, with occupancies of 0.50, 0.35 and 0.15. Both ClO_4^- ions are also disordered, one over two half-occupied sites and the other over three equally occupied orientations with a common fully occupied Cl atom. Lastly, the water molecule was also refined over three different sites, whose occupancies sum to 0.90. A whole molecule of water was included for the density and *F*(000) calculations, however, since this was more clearly resolved in the low temperature refinement from the same crystal. One of the ClO_4^- ions remains disordered in the low temperature structure, over two orientations with refined occupancies of 0.75:0.25. The water molecule, which hydrogen bonds to the disordered anion, is also distributed across two sites with the same refined occupancy ratio. All non-H atoms, including the disordered anion, were refined anisotropically. The disordered water H atoms were not located in the Fourier map at either temperature and are not included in the refinements, but are accounted for in the density and *F*(000) calculations. CCDC 1563027-1563028

Structure refinements of 1·sf. At 250 K one of the isopropylsulfanyl substitutents is disordered over three equally occupied orientations. Both anions are also disordered, over two and four equally occupied orientations respectively. At 100 K all this disorder had frozen out except for one ClO_4^- ion, for which two sites were resolved with occupancies of 0.65:0.35. There is no residual Fourier peak in either refinement in the region of the asymmetric unit occupied by the solvent. However, *SQUEEZE* analyses[3] at each temperature located solvent-accessible voids of 90-138 Å^3 per unit cell (45-69 Å^3 per solvent cavity), containing just 4-7 unresolved electrons per unit cell (1-2 electrons per formula unit). CCDC 1563029-1563030

Table S1 Experimental data for the crystal structures of **1[ClO$_4$]$_2$**·solv.

	1[ClO$_4$]$_2$·MeNO$_2$			**1[ClO$_4$]$_2$**·MeCN	
T [K]	250(2)	147(2)	100(2)	250(2)	142(2)
Molecular formula	$C_{29}H_{33}Cl_2FeN_{11}O_{10}S_2$	$C_{29}H_{33}Cl_2FeN_{11}O_{10}S_2$	$C_{29}H_{33}Cl_2FeN_{11}O_{10}S_2$	$C_{30}H_{33}Cl_2FeN_{11}O_8S_2$	$C_{30}H_{33}Cl_2FeN_{11}O_8S_2$
M_r	886.53	886.53	886.53	866.54	866.54
Crystal system	monoclinic	monoclinic	monoclinic	monoclinic	monoclinic
Space group	$P2_1/c$	$P2_1/c$	$P2_1/c$	$P2_1/c$	$P2_1/c$
a / Å	20.4604(4)	20.4690(2)	20.3076(10)	20.4279(4)	20.4344(2)
b / Å	11.9920(3)	11.9404(2)	11.8848(6)	11.9512(3)	11.8060(1)
c / Å	16.2456(4)	15.9241(2)	15.9663(8)	16.1688(5)	15.9788(2)
β / °	101.666(2)	101.789(1)	102.134(4)	100.738(2)	100.515(1)
V / Å^3	3903.70(16)	3809.88(9)	3767.4(3)	3878.29(17)	3790.13(7)
Z	4	4	4	4	4
μ / mm^{-1}	5.942	6.089	6.157	5.928	6.066
Measured reflections	18206	16738	14338	15386	14687
Independent reflections	7485	6672	7390	7395	6727
R_{int}	0.038	0.038	0.048	0.037	0.036
R_1, $I > 2\sigma(I)$[a]	0.055	0.045	0.070	0.053	0.038
wR_2, all data[b]	0.158	0.122	0.169	0.149	0.103

	1[ClO$_4$]$_2$·yMe$_2$CO		**1[ClO$_4$]$_2$**·H$_2$O		**1[ClO$_4$]$_2$**·sf	
T [K]	250(2)	147(2)	250(2)	100(2)	250(2)	118(2)
Molecular formula	$C_{30.10}H_{34.20}Cl_2FeN_{10}O_{8.70}S_2$	$C_{30.10}H_{34.20}Cl_2FeN_{10}O_{8.70}S_2$	$C_{28}H_{32}Cl_2FeN_{10}O_9S_2$	$C_{28}H_{32}Cl_2FeN_{10}O_9S_2$	$C_{28}H_{30}Cl_2FeN_{10}O_8S_2$	$C_{28}H_{30}Cl_2FeN_{10}O_8S_2$
M_r	866.14	866.14	866.54	866.54	825.49	825.49
Crystal system	monoclinic	monoclinic	monoclinic	monoclinic	monoclinic	monoclinic
Space group	$P2_1/c$	$P2_1/c$	$P2_1/c$	$P2_1/c$	$P2_1/c$	$P2_1/c$
a / Å	20.4915(4)	20.4826(3)	20.4689(5)	19.9722(7)	20.2860(6)	19.8888(8)
b / Å	11.9029(3)	11.8109(2)	11.8194(3)	11.9976(6)	11.7884(4)	12.0560(5)
c / Å	16.4898(4)	16.2096(2)	15.6562(5)	15.4592(7)	15.9103(6)	15.4109(8)
β / °	101.531(2)	101.419(1)	103.345(3)	103.466(4)	102.266(3)	104.145(4)
V / Å^3	3940.82(16)	3843.77(10)	3685.43(18)	3602.5(3)	3717.9(2)	3583.2(3)
Z	4	4	4	4	4	4
μ / mm^{-1}	5.839	5.986	6.233	6.376	6.145	6.376
Measured reflections	16507	16056	15400	15650	14219	13667
Independent reflections	7746	7596	6510	6385	6622	6343
R_{int}	0.037	0.038	0.049	0.043	0.045	0.042
R_1, $I > 2\sigma(I)$[a]	0.073	0.059	0.065	0.061	0.068	0.063
wR_2, all data[b]	0.221	0.167	0.190	0.171	0.203	0.176

[a] $R = \Sigma[\,|F_o| - |F_c|\,] / \Sigma|F_o|$ [b] $wR = [\Sigma w(F_o^2 - F_c^2) \;/\; \Sigma wF_o^4]^{1/2}$

Definitions of the Structural Parameters in Tables S2 and S6

Σ and Θ are defined as follows:

$$\Sigma = \sum_{i=1}^{12} |90 - \beta_i| \qquad \Theta = \sum_{j=1}^{24} |60 - \gamma_j|$$

where β_i are the twelve *cis*-N–Fe–N angles about the iron atom and γ_i are the 24 unique N–Fe–N angles measured on the projection of two triangular faces of the octahedron along their common pseudo-threefold axis (Scheme S1). Σ is a general measure of the deviation of a metal ion from an ideal octahedral geometry, while Θ more specifically indicates its distortion towards a trigonal prismatic structure. A perfectly octahedral complex gives $\Sigma = \Theta = 0$.[6,7]

Because the high-spin state of a complex has a much more plastic structure than the low-spin, this is reflected in Σ and Θ which are usually much larger in the high-spin state. The absolute values of these parameters depend on the metal/ligand combination in the compound under investigation, however.

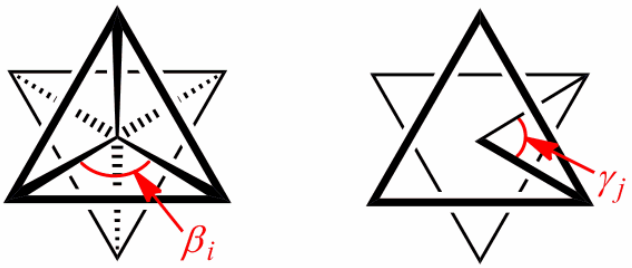

Scheme S1. Angles used in the definitions of the coordination distortion parameters Σ and Θ.

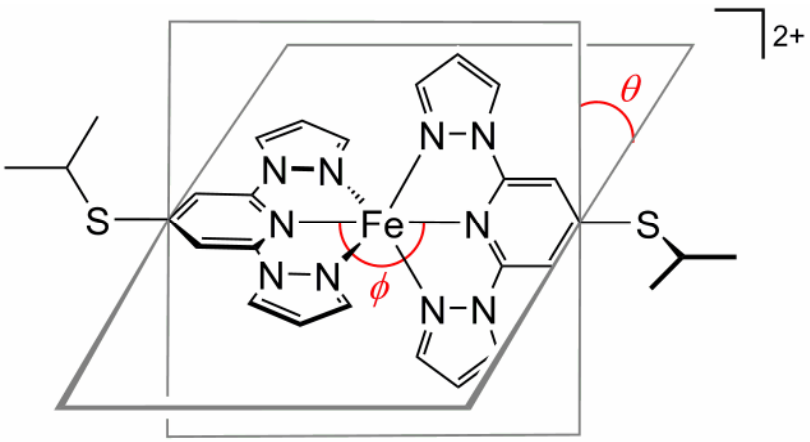

Scheme S2. Definition of the Jahn-Teller distortion parameters θ and ϕ.

These two parameters define the magnitude of an angular Jahn-Teller distortion, that is often observed in high-spin $[Fe(bpp)_2]^{2+}$ (bpp = 2,6-di{pyrazol-1-yl}pyridine) derivatives like $[FeL_2]^{2+}$ ($\theta \leq 90°$, $\phi \leq 180$ °).[8,9] They are also a useful indicator of the molecular geometry, in defining the disposition of the two ligands around the metal ion.

Spin-crossover can be inhibited if θ and ϕ deviate significantly from their ideal values, because the associated rearrangement to a more regular low-spin coordination geometry ($\theta \approx 90°$, $\phi \approx 180°$) cannot be accommodated by a rigid solid lattice.[9,10] Conversely, significant changes in θ and ϕ between the spin states can be associated with greater SCO cooperativity.[11]

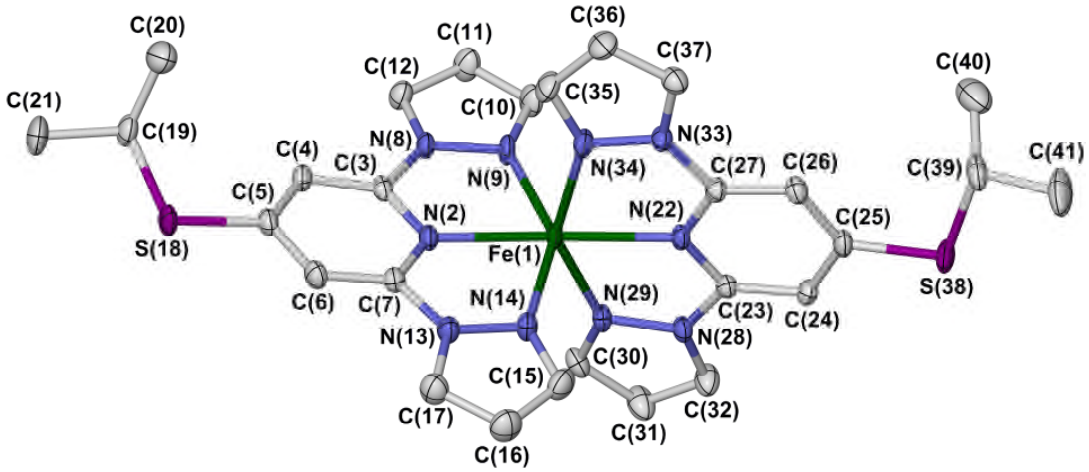

Figure S1. View of the $[FeL_2]^{2+}$ cation in **1[ClO$_4$]$_2$**·MeCN at 142 K, showing the atom numbering scheme employed in Table S2. Displacement ellipsoids are at the 50 % probability level, and H atoms have been omitted for clarity. Colour code: C, white; Fe, green; N, blue; S, purple.

Table S2 Selected bond distances and angular parameters for the **1[ClO$_4$]$_2$**·solv compounds at different temperatures (Å, °). See Fig. S1 for the atom numbering scheme. The corresponding data for the **1[BF$_4$]$_2$**·solv series are given in ref. 2.

Σ and Φ are indices characteristic for the spin state of the complex,[6,7] while φ and θ are measures of the deviation of the complex molecule from idealised D_{2d} symmetry (see above).[8,9] Typical values of these parameters for complexes related to $[FeL_2]^{2+}$ are given in ref. 8.

	1[ClO$_4$]$_2$·MeCN	**1[ClO$_4$]$_2$**·MeCN	**1[ClO$_4$]$_2$**·MeNO$_2$	**1[ClO$_4$]$_2$**·MeNO$_2$	**1[ClO$_4$]$_2$**·MeNO$_2$	
T [K]	250(2)	142(2)	250(2)	147(2)	100(2)	
Spin state[a]	HS	HS	HS	HS	Mixed[b]	
Fe(1)–N(2)	2.139(2)	2.1356(16)	2.134(2)	2.128(2)	2.052(4)	
Fe(1)–N(9)	2.178(3)	2.1815(18)	2.180(3)	2.170(2)	2.099(4)	
Fe(1)–N(14)	2.215(3)	2.2115(19)	2.219(3)	2.215(2)	2.134(4)	
Fe(1)–N(22)	2.129(2)	2.1295(16)	2.127(2)	2.123(2)	2.044(4)	
Fe(1)–N(29)	2.179(3)	2.1772(18)	2.176(3)	2.172(2)	2.097(5)	
Fe(1)–N(34)	2.173(3)	2.1732(18)	2.177(3)	2.168(2)	2.087(3)	
Σ	156.5(3)	155.7(2)	154.5(4)	153.2(3)	130.5(5)	
Θ	485	484	479	476	412	
ϕ	167.2(1)	167.05(7)	168.7(1)	168.95(8)	170.53(14)	
θ	86.29(3)	86.75(2)	85.15(3)	85.93(2)	86.06(4)	
	1[ClO$_4$]$_2$·*y*Me$_2$CO	**1[ClO$_4$]$_2$**·*y*Me$_2$CO	**1[ClO$_4$]$_2$**·H$_2$O	**1[ClO$_4$]$_2$**·H$_2$O	**1[ClO$_4$]$_2$**·sf	**1[ClO$_4$]$_2$**·sf
T [K]	250(2)	147(2)	250(2)	100(2)	250(2)	118(2)
Spin state[a]	HS	HS	HS	LS	HS	LS
Fe(1)–N(2)	2.139(3)	2.133(2)	2.129(3)	1.911(3)	2.144(3)	1.903(3)
Fe(1)–N(9)	2.181(4)	2.172(3)	2.169(4)	1.985(3)	2.157(4)	1.987(3)
Fe(1)–N(14)	2.215(4)	2.210(3)	2.213(4)	1.982(3)	2.233(4)	1.983(3)
Fe(1)–N(22)	2.125(3)	2.121(2)	2.108(3)	1.907(3)	2.111(3)	1.903(3)
Fe(1)–N(29)	2.180(3)	2.175(3)	2.189(4)	1.988(3)	2.181(4)	1.991(3)
Fe(1)–N(34)	2.188(4)	2.177(3)	2.171(4)	1.965(3)	2.176(4)	1.965(3)
Σ	156.6(5)	154.7(4)	151.1(5)	89.6(4)	153.9(5)	90.2(5)
Θ	488	482	471	292	480	295
ϕ	166.1(1)	166.8(1)	169.20(13)	175.54(12)	164.55(14)	174.47(14)
θ	84.15(4)	86.22(3)	87.13(4)	88.61(3)	85.08(4)	88.01(3)

[a]HS = high-spin, LS = low-spin, mixed = a mixed high-spin/low-spin population. [b]The Σ and Φ values imply the crystal does not have a pure spin-state population at this temperature, which is consistent with magnetic susceptibility data (Fig. 1, main article).

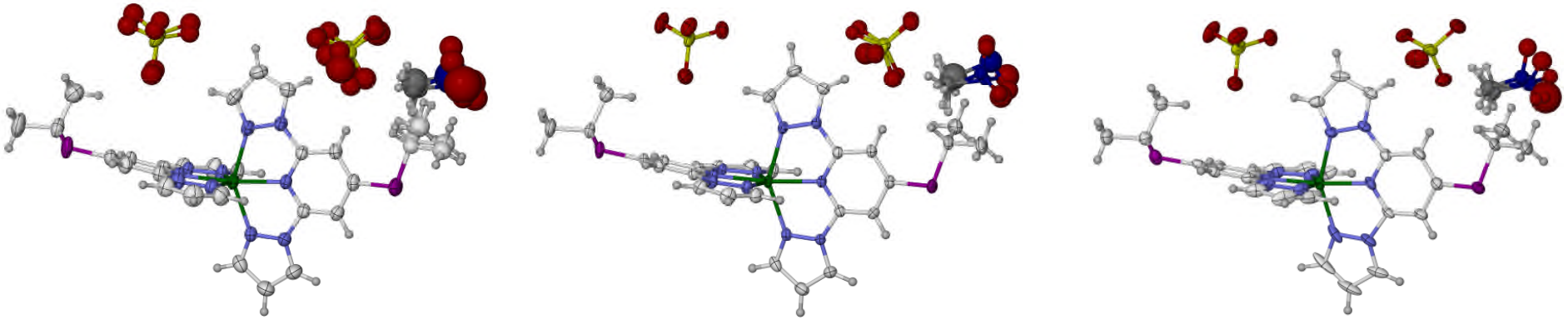

T = 250 K, high-spin

T = 147 K, high-spin

T = 100 K,
mixed high/low-spin state population

Figure S2 Comparison of the disorder in the asymmetric unit of **1[ClO$_4$]$_2$**·MeNO$_2$ at different temperatures. Atomic displacement ellipsoids are drawn at the 50 % probability level.

Colour code: C{complex}, white; C{solvent}, dark gray; H, pale gray; Cl, yellow; Fe, green; N{complex}, pale blue; N{solvent}, dark blue; O, red; S, purple.

1[ClO$_4$]$_2$·MeCN

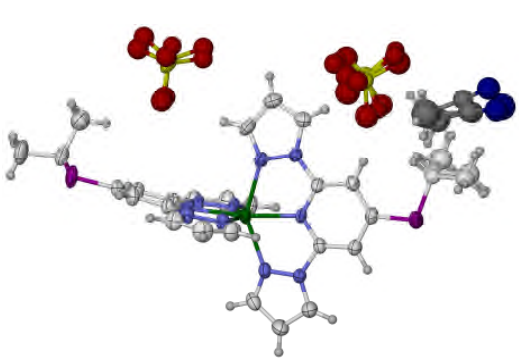

T = 250 K, high-spin

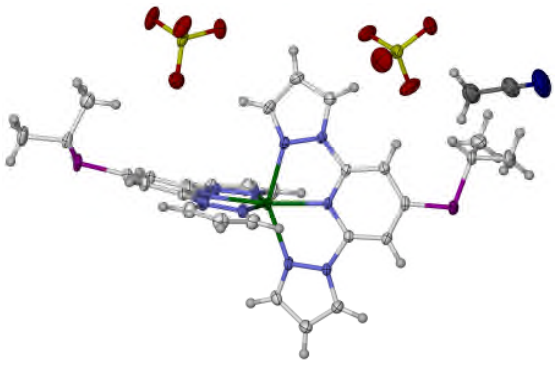

T = 142 K, high-spin

1[ClO$_4$]$_2$·*y*Me$_2$CO
(*y* ≈ 0.75)

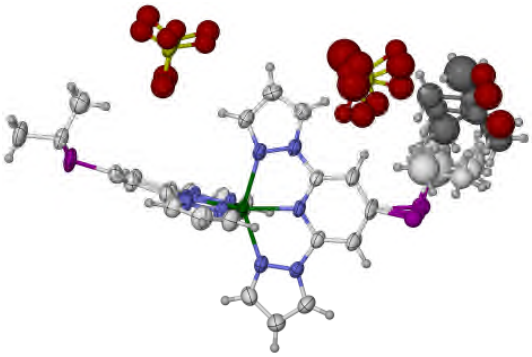

T = 250 K, high-spin

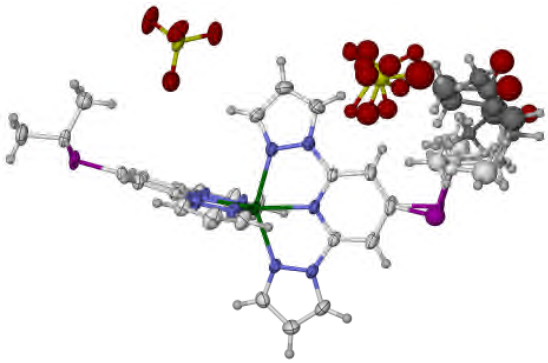

T = 147 K, high-spin

1[ClO$_4$]$_2$·H$_2$O

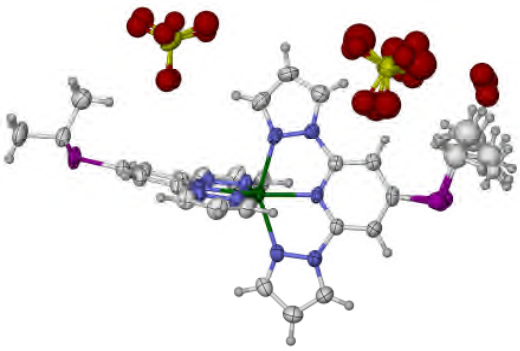

T = 250 K, high-spin

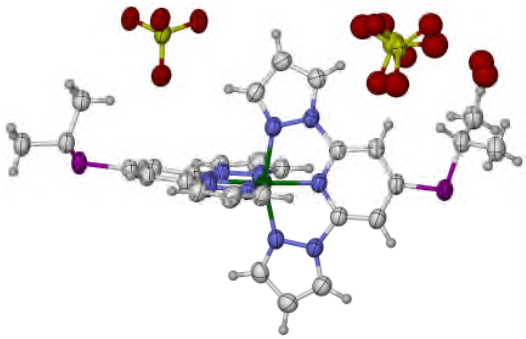

T = 100 K, high-spin

1[ClO$_4$]$_2$·sf

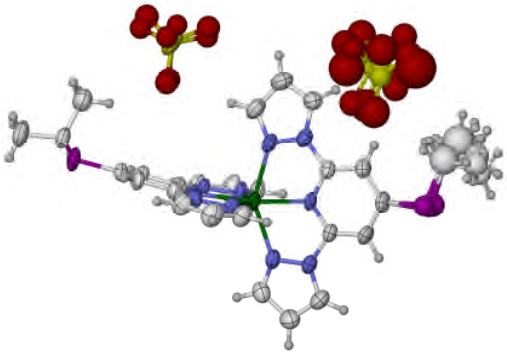

T = 250 K, high-spin

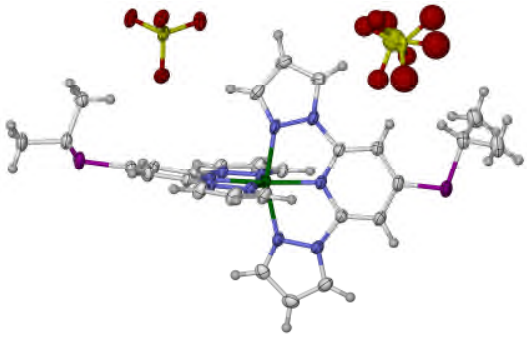

T = 118 K, low-spin

Figure S3 Comparison of the disorder in the asymmetric unit of the other **1[ClO$_4$]$_2$**·solv structures. Atomic displacement ellipsoids are drawn at the 50 % probability level.

Colour code: C{complex}, white; C{solvent}, dark gray; H, pale gray; Cl, yellow; Fe, green; N{complex}, pale blue; N{solvent}, dark blue; O, red; S, purple.

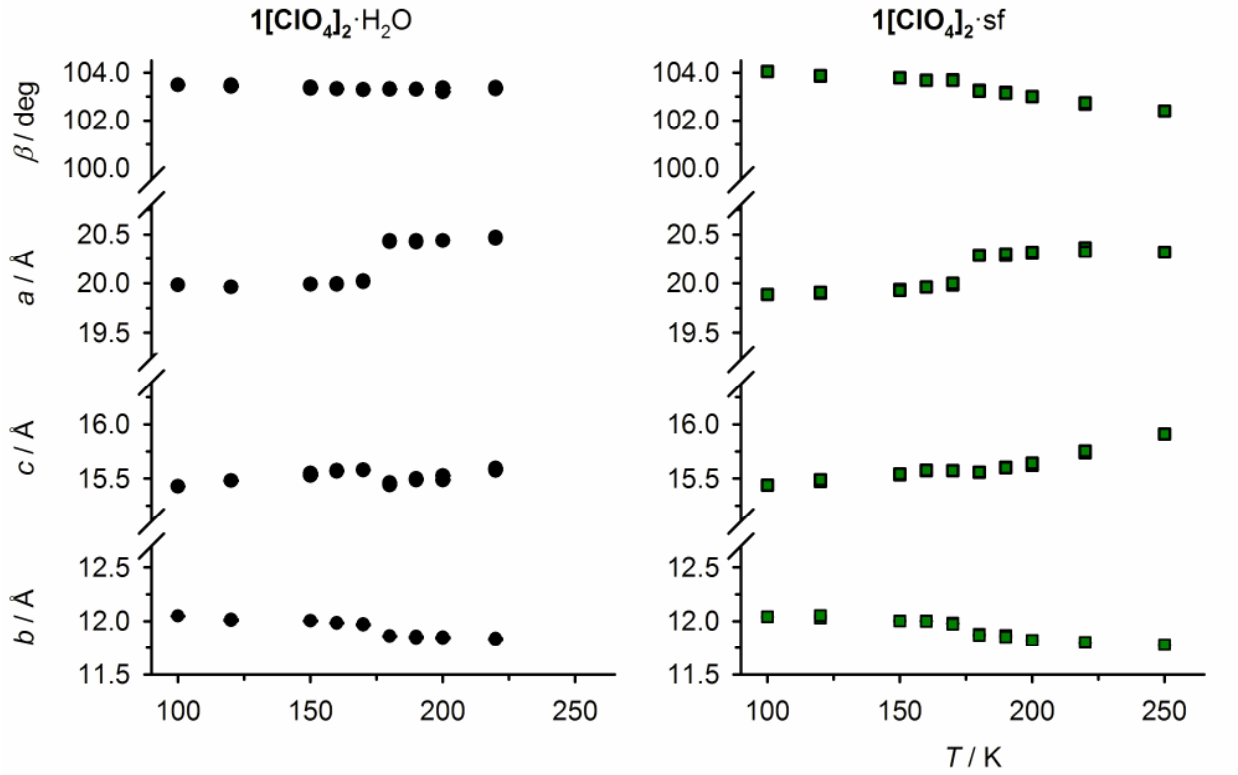

Figure S4. Variable temperature unit cell parameters for **1[ClO$_4$]$_2$**·H$_2$O and **1[ClO$_4$]$_2$**·sf, showing their abrupt spin-transitions (Table S3). Data are shown on both cooling and warming temperature cycles. Error bars are shown, but are mostly smaller than the symbols on the graph.

These data were obtained from the same crystals, during the same experiments, as the full structure determinations for those two compounds. Hence the $T_{½}$ value for **1[ClO$_4$]$_2$**·sf is reliable, despite its being within experimental error of $T_{½}$ for **1[ClO$_4$]$_2$**·H$_2$O.

A discontinuity associated with SCO for **1[ClO$_4$]$_2$**·H$_2$O occurs between 170-180 K, in excellent agreement with $T_{½}$ = 175 K for this compound from the magnetic susceptibility data (main article). The synthesis of a bulk sample of **1[ClO$_4$]$_2$**·sf for magnetic measurements, by annealing methods, was not pursued on safety grounds. However its crystallographic SCO temperature of 175 ±5 K from these data is similar to that of **1[BF$_4$]$_2$**·sf ($T_{½}$ = 185 K from magnetic measurements, or 165 ±5 K from unit cell data).[2]

Table S3 Variable temperature unit cell data for **1[ClO$_4$]$_2$**·H$_2$O and **1[ClO$_4$]$_2$**·sf (Figure S4).

	T / K	a / Å	b / Å	c / Å	β / °	V / Å^3
1[ClO$_4$]$_2$·H$_2$O	220	20.459(20	11.8398(12)	15.576(3)	103.320(13)	3671.4(9)
	200	20.439(4)	11.853(2)	15.487(5)	103.21(2)	3652.67(15)
	190	20.440(2)	11.8599(11)	15.486(3)	103.299(12)	3653.4(9)
	180	20.440(3)	11.8650(13)	15.439(3)	103.323(13)	3643.3(10)
	170	20.025(4)	11.9758(18)	15.582(5)	103.29(2)	3636.8(14)
	160	19.985(3)	11.9881(15)	15.565(4)	103.319(17)	3628.8(12)
	150	19.991(5)	12.0033(17)	15.528(4)	103.35(2)	3625.3(14)
	120	19.963(3)	12.0087(19)	15.481(5)	103.48(2)	3608.9(15)
	100	19.983(5)	12.0489(13)	15.427(4)	103.489(16)	3612.0(11)
	120	19.965(4)	12.020(2)	15.468(5)	103.42(2)	3610.5(16)
	150	19.989(4)	12.0057(19)	15.552(5)	103.40(2)	3630.6(14)
	160	19.996(5)	11.984(2)	15.576(6)	103.33(3)	3631.8(18)
	170	20.014(5)	11.966(3)	15.579(5)	103.30(2)	3631.1(17)
	180	20.427(3)	11.8602(15)	15.462(4)	103.305(17)	3645.5(12)
	190	20.422(7)	11.844(3)	15.500(7)	103.31(3)	3648(2)
	200	20.438(3)	11.8411(16)	15.527(4)	103.373(17)	3655.7(12)
	220	20.472(5)	11.829(2)	15.598(5)	103.38(2)	3674.7(15)
	220	20.459(2)	11.8398(12)	15.576(3)	103.320(13)	3671.4(9)
1[ClO$_4$]$_2$·sf	220	20.364(5)	11.798(5)	15.737(5)	102.69(3)	3689(2)
	200	20.305(3)	11.825(4)	15.624(4)	103.02(2)	3654.9(17)
	190	20.286(2)	11.869(3)	15.603(3)	103.182(12)	3657.8(11)
	180	20.290(2)	11.880(2)	15.558(3)	103.277(13)	3649.9(11)
	170	19.983(2)	11.985(2)	15.573(2)	103.708(11)	3623.3(9)
	160	19.965(3)	12.004(4)	15.574(4)	103.681(18)	3626.6(15)
	150	19.938(2)	12.005(2)	15.537(2)	103.789(11)	3611.5(10)
	120	19.901(2)	12.032(3)	15.476(3)	103.856(14)	3597.9(12)
	100	19.886(2)	12.042(3)	15.439(2)	104.048(12)	3586.63(10)
	120	19.910(3)	12.055(4)	15.489(3)	103.867(17)	3609.14(15)
	150	19.928(2)	12.003(3)	15.544(3)	103.792(14)	3610.5(11)
	160	19.961(4)	12.001(4)	15.578(4)	103.68(2)	3625.9(16)
	170	20.000(2)	11.975(2)	15.5750(14)	103.690(8)	3624.15(6)
	180	20.284(3)	11.870(3)	15.561(3)	103.237(14)	3646.9(12)
	190	20.304(2)	11.854(2)	15.601(2)	103.147(11)	3656.6(9)
	200	20.317(4)	11.825(4)	15.643(4)	103.00(2)	3661.7(18)
	220	20.325(3)	11.807(3)	15.755(3)	102.743(15)	3687.5(12)
	250	20.319(2)	11.779(3)	15.912(2)	102.408(12)	3719.2(12)

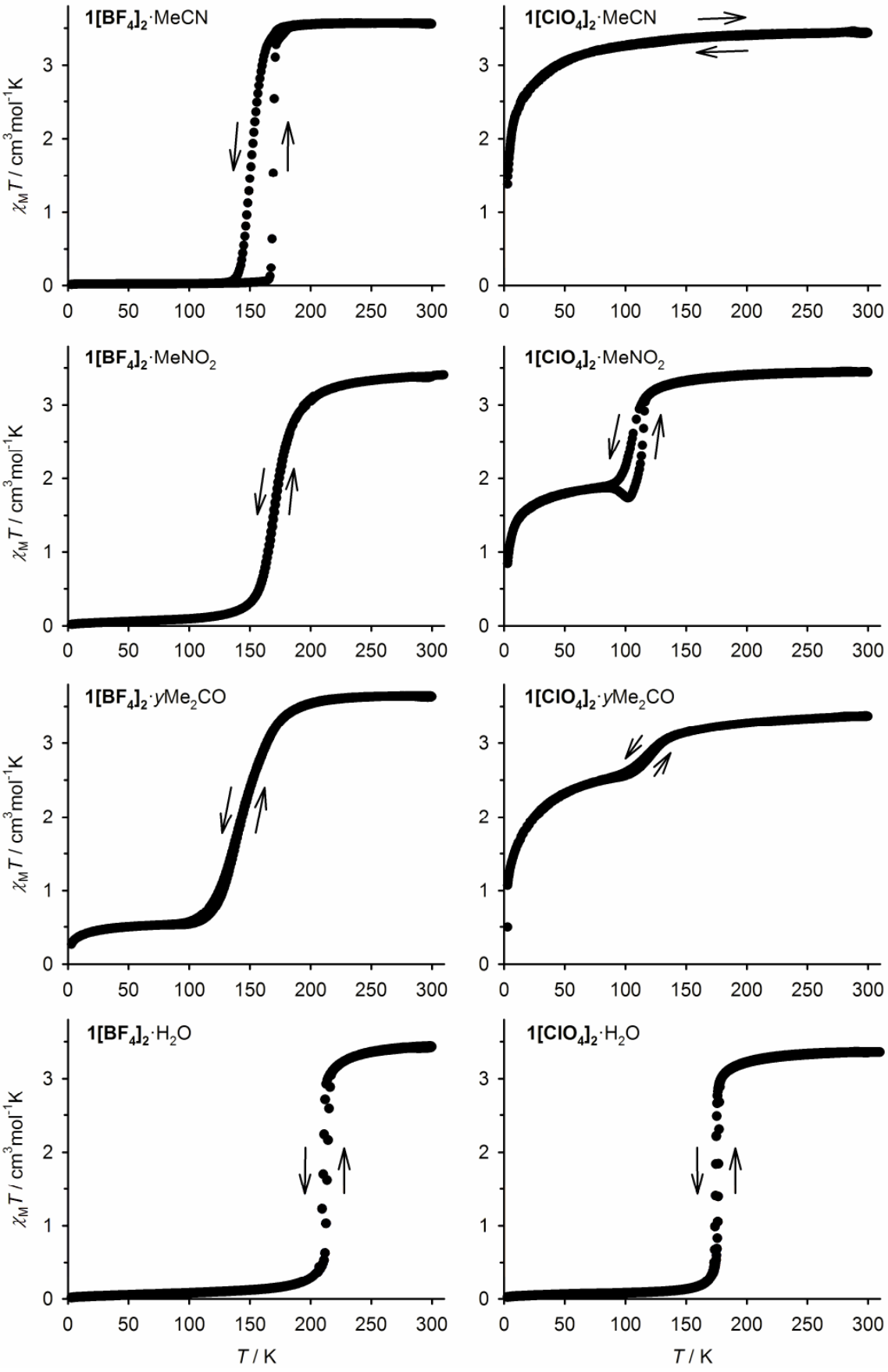

Figure S5. Comparison of the magnetic susceptibility data of materials from the **1[BF$_4$]$_2$**·solv (left) and **1[ClO$_4$]$_2$**·solv (right) series, at a scan rate of 5 Kmin^{-1}. Data for **1[BF$_4$]$_2$**·solv are taken from ref. 2.

Data in Figure 1 of the main article were measured at the slower scan rate of 0.4 Kmin^{-1}.

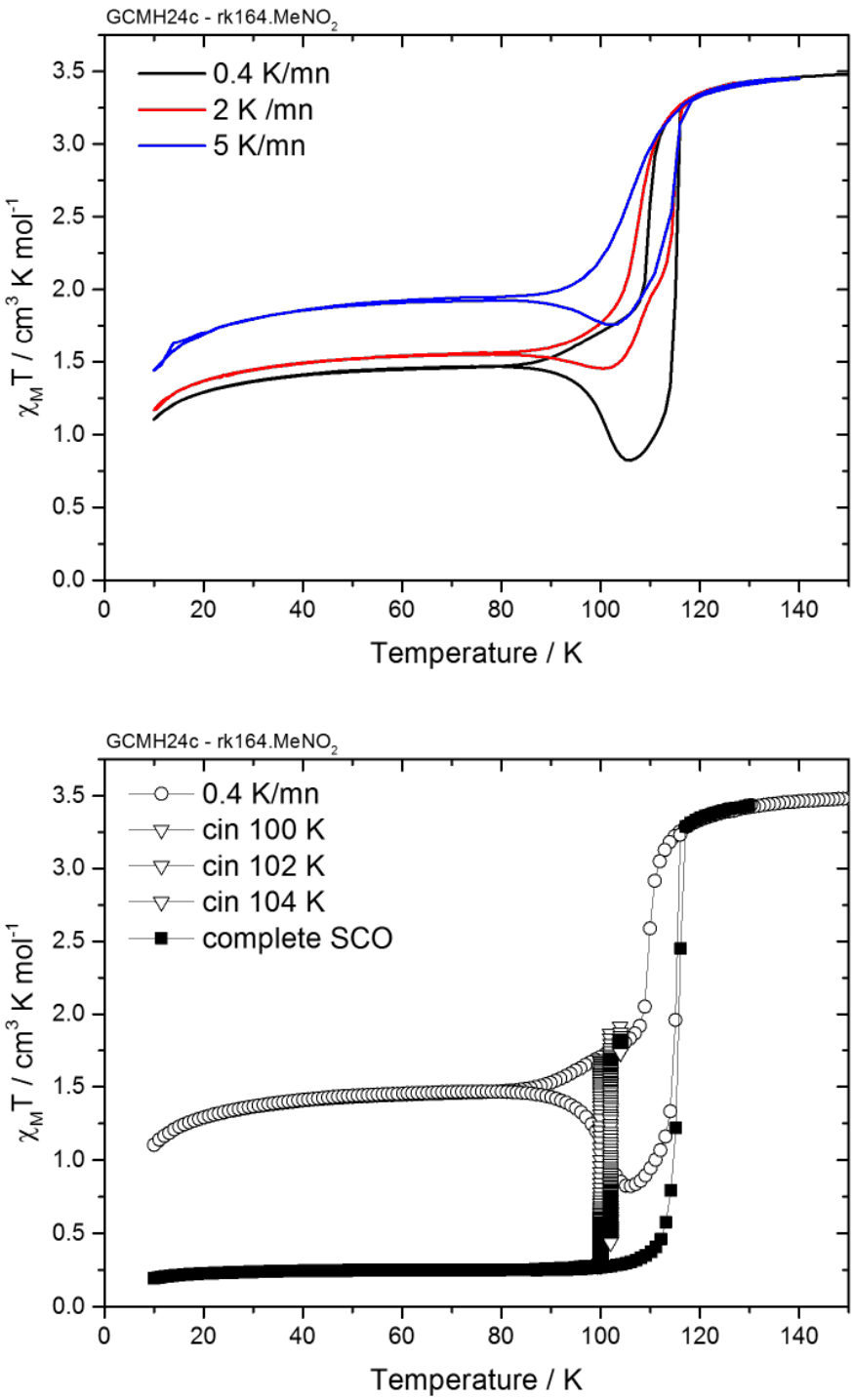

Figure S6. The slow SCO kinetics shown by **1[ClO$_4$]$_2$**·MeNO$_2$ in the SQUID magnetometer.

Top: measurements at three different scan rates, showing the increased high→low-spin conversion at slower scan rates.

Bottom. the change in $\chi_M T$ as the sample is poised at three different temperatures for 60-80 minutes (▽), allowing it to relax to its thermodynamic spin-state population at each temperature. The fully low-spin material was achieved after 80 minutes at 100 K, which was then subjected to a full cooling/warming cycle (■).

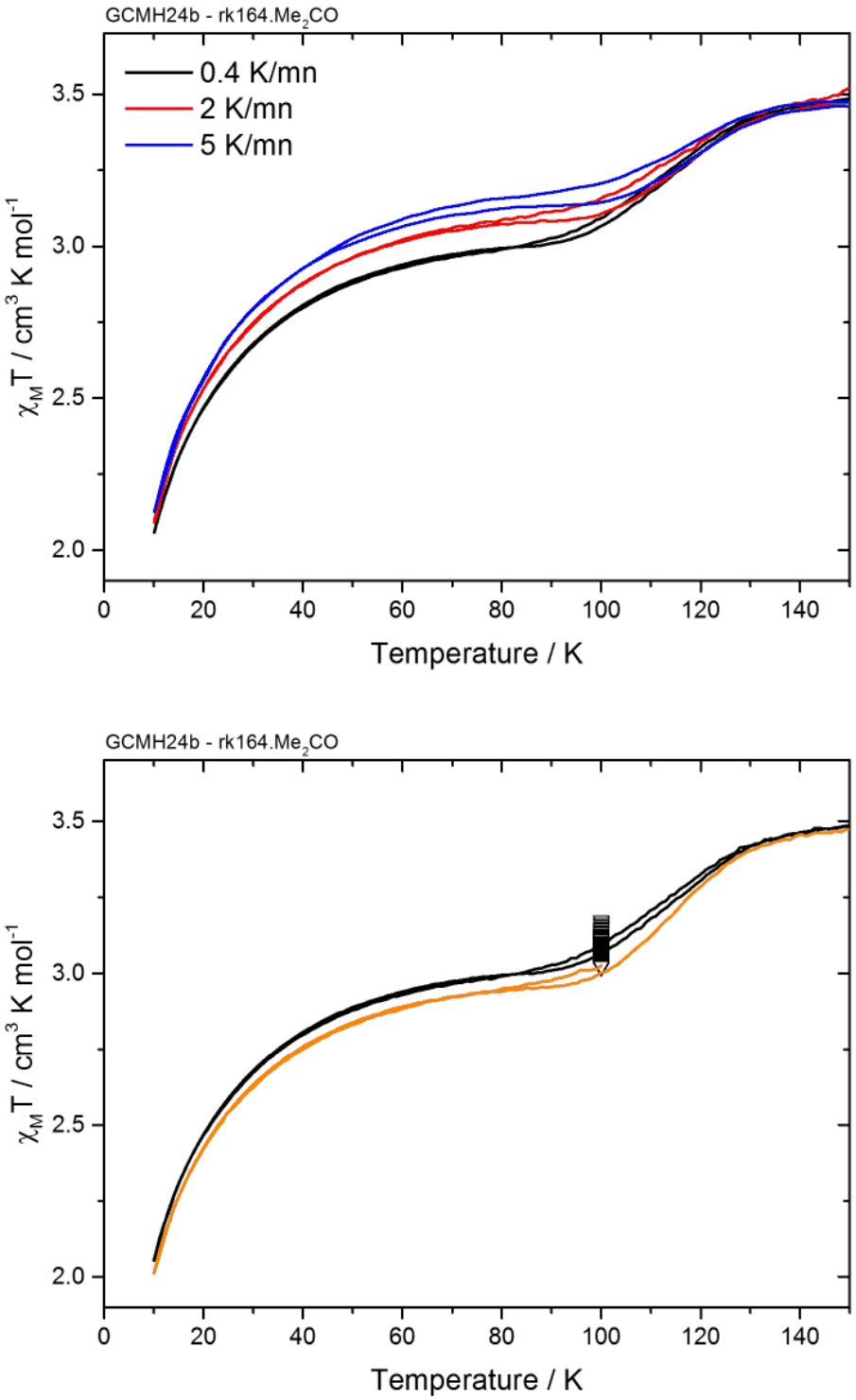

Figure S7. The slow SCO kinetics shown by **1[ClO$_4$]$_2$**·Me$_2$CO in the SQUID magnetometer.

Top: measurements at three different scan rates, showing a slightly increased high→low-spin conversion at slower scan rates.

Bottom. the change in $\chi_M T$ as the sample is poised at 100 K for 520 minutes (▽), allowing it to relax to its thermodynamic spin-state population which was then subjected to a full cooling/warming cycle (orange line).

In contrast to **1[ClO$_4$]$_2$**·MeNO$_2$, the dependence of $\chi_M T$ on scan rate in these data is extremely small. Therefore, these $\chi_M T$ data accurately reflect the thermodynamic spin-state population of **1[ClO$_4$]$_2$**·Me$_2$CO near 100 K.

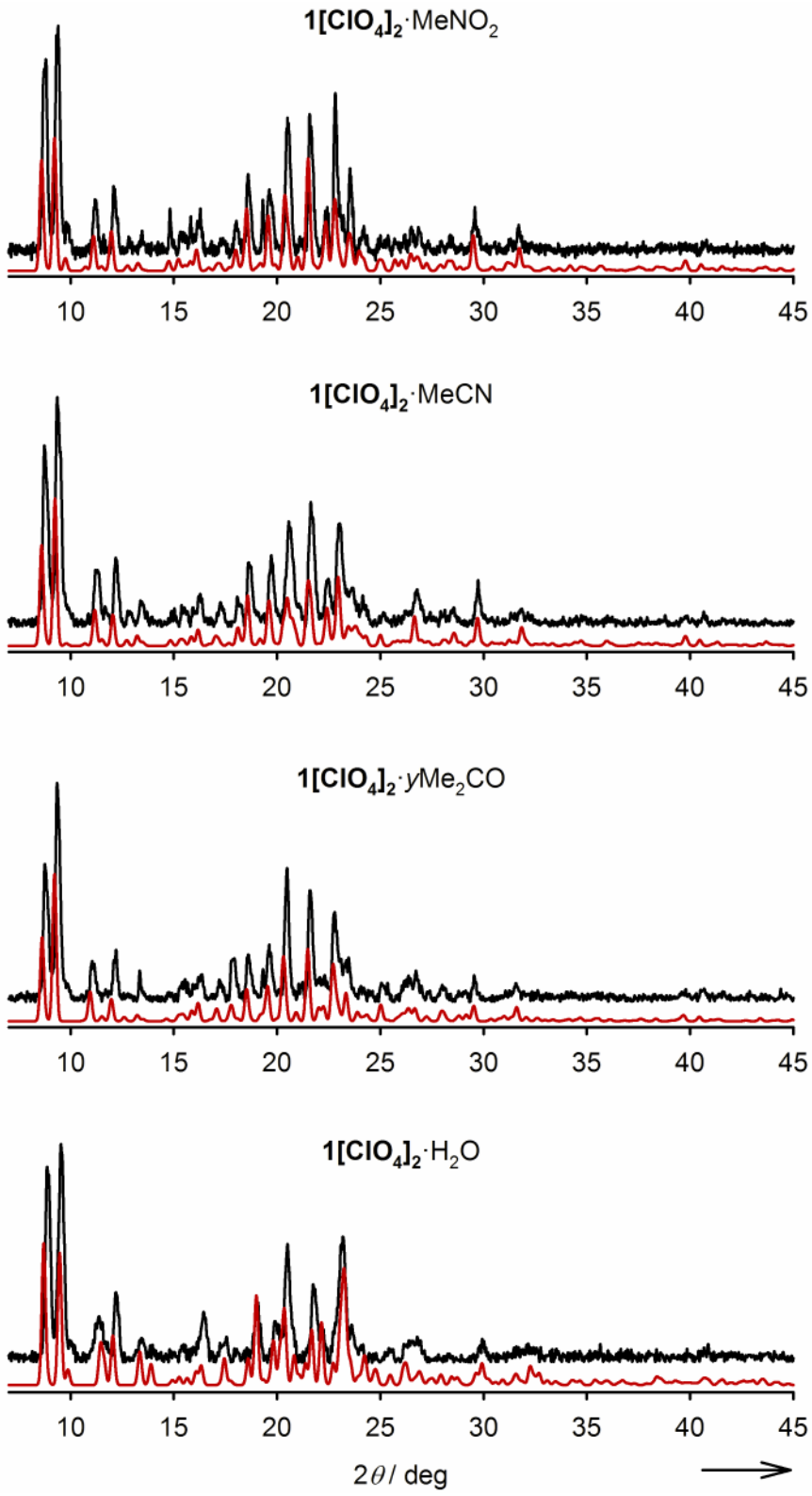

Figure S8. Experimental (black) and simulated (red) room temperature X-ray powder diffraction patterns for the **1[ClO$_4$]$_2$**·solv materials.

Photomagnetic and Photocrystallographic Data from $1[BF_4]_2$·solv and $1[ClO_4]_2$·solv

Experimental

Photomagnetic measurements

Photomagnetic measurements were performed using a set of photodiodes coupled via an optical fibre to the cavity of a MPMS-55 Quantum Design SQUID magnetometer operating at 2000 G. The powder sample was prepared in a thin layer (~0.1 mg) to promote full penetration of the irradiated light. The sample mass was obtained by comparison with the thermal spin transition curve measured on a larger, accurately weighed polycrystalline sample. The sample was first slow cooled to 10 K, ensuring that potential trapping of HS species at low temperatures did not occur. Irradiation was carried out at a set wavelength and the power of the sample surface was adjusted to 5 mW cm^{-2}. Once photo-saturation was reached, irradiation was ceased and the temperature increased at a rate of 0.3 K min^{-1} to ~100 K and the magnetisation measured every 1 K to determine the *T*(LIESST) value given by the minimum of the $\delta\chi_M T/\delta T$ *vs T* curve for the relaxation.[12]

The *T*(LIESST) value describes the limiting temperature above which the light-induced magnetic high-spin information is erased in a SQUID cavity. In the absence of irradiation, the magnetisation was also measured over the temperature range 10–290 K to follow the thermal spin transition and to obtain a low temperature baseline. Kinetic studies of LIESST relaxation were performed by irradiating the sample at 10 K until photo-saturation, then, under constant irradiation the sample was warmed to a desired temperature around the *T*(LIESST) region. At the desired temperature, irradiation is stopped and the decay of the magnetisation signal was followed for several hours, or until complete relaxation back to the low-spin baseline.

Single crystal X-ray structure determinations of $1[BF_4]_2$·solv at low temperature, or under irradiation

Crystals of $\mathbf{1[BF_4]_2}\cdot MeNO_2$, $\mathbf{1[BF_4]_2}\cdot$MeCN and $\mathbf{1[BF_4]_2}\cdot H_2O$ were prepared as previously described.[2] All diffraction data were collected with an Oxford Diffraction Xcalibur3 diffractometer, using monochromated Mo-$K\alpha$ radiation (λ = 0.71073 Å). The diffractometer was fitted with a liquid nitrogen Oxford Cyosystems 700 series low-temperature device for measurements down to 80 K, or with a Helijet Oxford Diffraction helium cryostat for measurements below 30 K. Experimental details of the structure determinations are given in Table S4. The structures were solved by dual-space direct methods (*SHELXT*[4]), and developed by full least-squares refinement on F^2 (*SHELXL*[4]). Crystallographic figures were prepared using *X-SEED*.[5]

Structure refinement details for $1[BF_4]_2$·solv

Unless otherwise stated, all non-H atoms were refined anisotropically, and H atoms were placed in calculated positions and refined using a riding model. Disordered anions were modelled using fixed B–F distance restraints.

Structure refinements of $1[BF_4]_2\cdot MeNO_2$. Three different crystals of this compound were measured, which all showed the same phase behavior. The best data obtained are presented in this paper, which were collected from two different crystals. The first crystal was measured at 100 K, and the second crystal was used for measurements at 15 K before and after irradiation with 660nm *cw*-laser at ~3.5mW laser power. Each structure adopts a different crystallographic phase.

In phase 1 (higher symmetry low-spin) at 100 K, the F atoms in both anions are disordered over two sites, with refined occupancy ratios of 0.82:0.18, and 0.74:0.26. Disorder in the $MeNO_2$ molecule was also evident, which was treated using partial O atom environments. No disorder is present in phase 2 (lower symmetry low-spin due to cell tripling along *b*-axis), but one of the two unique solvent sites in phase 3 (high-spin) is also disordered and was modelled in the same way. In case of phase 3 the reflections conditions have been fulfilled only for 2_1 screw axis, *n*-glide plane is no longer present. Therefore the non-centrosymmetric space group, $P2_1$ has been assigned. In addition, phase 3 has been treated with an inversion twin due to possible domain formation or crystal breaking upon irradiation at 15 K. Weak diffraction at 15 K and symmetry breaking upon photoexcitation can explain the higher Flack parameter in phase 3.

CCDC 1564670-1564672.

Structure refinements of $1[BF_4]_2\cdot$MeCN. An initial experiment at 15 K afforded the thermally trapped high-spin form of the compound. Either the crystal was already exposed to light during the mounting process, or it was cooled too quickly in the helium stream to undergo thermal SCO. In any case, due to technological limitations of the Helijet cryostat the crystal could not be warmed above its higher *T*(LIESST) temperature (108 K) to ensure complete relaxation to its low-spin state. Therefore, a structure of the low-spin state of this compound at 15 K was not obtained.

The LIESST process was instead monitored in a new crystal, at the higher temperature of 85 K. For photoexcitation 660nm *cw*-laser was used at ~2mW laser power. In the low spin form at 85 K, one BF_4^- ion is disordered over two sites, with refined occupancies of 0.52:0.48, which are related by rotation about one B–F bond. No disorder is present in the two high-spin structures.

CCDC 1564667-1564669.

Structure refinements of 1[BF_4]$_2$·H_2O. The structure was determined at 20 K, before and after irradiation for the same crystal. For photoexcitaiton 660nm *cw*-laser was used at ~3.5mW laser power. One BF_4^- ion is disordered in both structures, over two sites with an approximate 0.95:0.05 occupancy ratio. Pairs of partial F-atoms were constrained to the same anisotropic displacement ellipsoids with the *SHELXL EADP* instruction and where necessary, restrained with the *SHELXL ISOR* instruction. The water H atoms were located in the Fourier map and allowed to refine, with U_{iso} constrained to 1.5x U_{eq}(O). CCDC 1564665-1564666.

Table S4 Experimental data for the crystal structures of **1[BF$_4$]$_2$**·solv under irradiation, or thermal trapping.

	1[BF$_4$]$_2$·MeNO$_2$			**1[BF$_4$]$_2$**·H$_2$O	
T [K]	100(2)	15(2)	15(2)	20(2)	20(2)
	Phase 1, low-spin	Phase 2, low-spin	Phase 3, high-spin	Phase 1, low-spin	Phase 1, high-spin
Molecular formula	$C_{29}H_{33}B_2F_8FeN_{11}O_2S_2$	$C_{29}H_{33}B_2F_8FeN_{11}O_2S_2$	$C_{29}H_{33}B_2F_8FeN_{11}O_2S_2$	$C_{28}H_{32}B_2F_8FeN_{10}OS_2$	$C_{28}H_{32}B_2F_8FeN_{10}OS_2$
M_r	861.25	861.25	861.25	818.22	818.22
Crystal system	monoclinic	monoclinic	monoclinic	monoclinic	monoclinic
Space group	$P2_1/c$	$P2_1/c$	$P2_1$	$P2_1/c$	$P2_1/c$
a / Å	19.7391(7)	19.7255(5)	20.2896(5)	19.7442(10)	20.2276(5)
b / Å	11.9252(4)	35.2106(8)	12.0942(3)	12.1364(5)	11.8791(3)
c / Å	16.0160(5)	16.0710(4)	15.3831(4)	15.0558(9)	15.0082(4)
β / °	100.942(3)	100.706(2)	101.088(2)	103.004(5)	102.531(2)
V / Å^3	3701.5(2)	10967.8(5)	3704.34(16)	3515.2(3)	3520.35(16)
Z	4	12	4	4	4
μ / mm^{-1}	0.607	0.614	0.606	0.632	0.631
Measured reflections	17525	53607	16837	18249	36302
Independent reflections	8888	23910	11529	7671	7685
R_{int}	0.072	0.059	0.027	0.070	0.084
R_1, $I > 2\sigma(I)$[a]	0.067	0.057	0.033	0.052	0.047
wR_2, all data[b]	0.094	0.124	0.073	0.098	0.101
Flack parameter	–	–	0.483(15)	–	–

	1[BF$_4$]$_2$·MeCN		
T [K]	85(2)	85(2)	15(2)
	Phase 1, low-spin	Phase 1, high-spin	Phase 1, high-spin
Molecular formula	$C_{30}H_{33}B_2F_8FeN_{11}S_2$	$C_{30}H_{33}B_2F_8FeN_{11}S_2$	$C_{30}H_{33}B_2F_8FeN_{11}S_2$
M_r	841.26	841.26	841.26
Crystal system	monoclinic	monoclinic	monoclinic
Space group	$P2_1/c$	$P2_1/c$	$P2_1/c$
a / Å	19.5906(3)	20.2089(3)	20.2280(5)
b / Å	12.3086(2)	11.8753(2)	11.8526(4)
c / Å	15.6311(2)	15.6161(3)	15.5284(4)
β / °	100.6220(10)	99.4110(10)	99.208(2)
V / Å^3	3704.59(10)	3697.22(11)	3675.03(18)
Z	4	4	4
μ / mm^{-1}	0.600	0.602	0.605
Measured reflections	34450	34512	19748
Independent reflections	8066	8048	7998
R_{int}	0.033	0.034	0.052
R_1, $I > 2\sigma(I)$[a]	0.034	0.038	0.051
wR_2, all data[b]	0.079	0.092	0.128

[a] $R = \Sigma[|F_o| - |F_c|] / \Sigma|F_o|$ [b] $wR = [\Sigma w(F_o^2 - F_c^2) \ / \ \Sigma wF_o^4]^{1/2}$

Table S5 *T*(LIESST) data for compounds from the $[Fe(bpp)_2]X_2$ series (Scheme S3), which are plotted in Figure 2 (main article). Only data from our group are included for consistency, since *T*(LIESST) is sensitive to the conditions of measurement.[13] LIESST data in related compounds from other researchers are also available.[14]

	$T_{½}$ / K	*T*(LIESST) / K	ref
$[Fe(bpp)_2][BF_4]_2$	260	81	15
$[Fe(bpp)_2]_x[Ru(terpy)_2]_{1-x}[BF_4]_2$ (x = 0.95)	260	79	16
$[Fe(bpp)_2]_x[Ru(terpy)_2]_{1-x}[BF_4]_2$ (x = 0.75)	258	75.5	16
$[Fe(bpp)_2]_x[Ru(terpy)_2]_{1-x}[BF_4]_2$ (x = 0.57)	260	75	16
$[Fe(bpp)_2]_x[Ru(terpy)_2]_{1-x}[BF_4]_2$ (x = 0.47)	264	73	16
$[Fe(bpp)_2]_x[Ru(terpy)_2]_{1-x}[BF_4]_2$ (x = 0.28)	273	69	16
$[Fe(bpp)_2]_x[Co(terpy)_2]_{1-x}[BF_4]_2$ (x = 0.97)	261	80	16
$[Fe(bpp)_2]_x[Co(terpy)_2]_{1-x}[BF_4]_2$ (x = 0.85)	256	78	16
$[Fe(bpp)_2]_x[Co(terpy)_2]_{1-x}[BF_4]_2$ (x = 0.76)	253	77	16
$[Fe(bpp^{3\text{-}Me})_2][BF_4]_2$	115	85	17
$[Fe(bpp^{4\text{-}Me})_2][ClO_4]_2$	233	84	15
$[Fe(bpp^{4\text{-}Cl})_2][BF_4]_2$	202	100	18
$[Fe(bpp^{4\text{-}Br})_2][BF_4]_2$	253	82	18
$[Fe(bpp^{Me})_2][BF_4]_2$	206	87	11
$[Fe(bpp^{Me})_2][ClO_4]_2$	188	112	11
$[Fe(bpp^{CH2OH})_2][BF_4]_2$	271	70	15
$[Fe(bpp^{CH2OH})_2][ClO_4]_2$	284	65	15
$[Fe(bpp^{Br})_2][BF_4]_2$	307	70	19
$[Fe(bpp^{I})_2][BF_4]_2$	332	65	19
$[Fe(bpp^{SMe})_2][BF_4]_2$	269	80	19
$[Fe(bpyz)_2][BF_4]_2$	220	91	15
$[Fe(bpyz)_2][ClO_4]_2$	201	100	15
$[Fe(bpyz^{4\text{-}Me})_2][BF_4]_2$	242	93	20

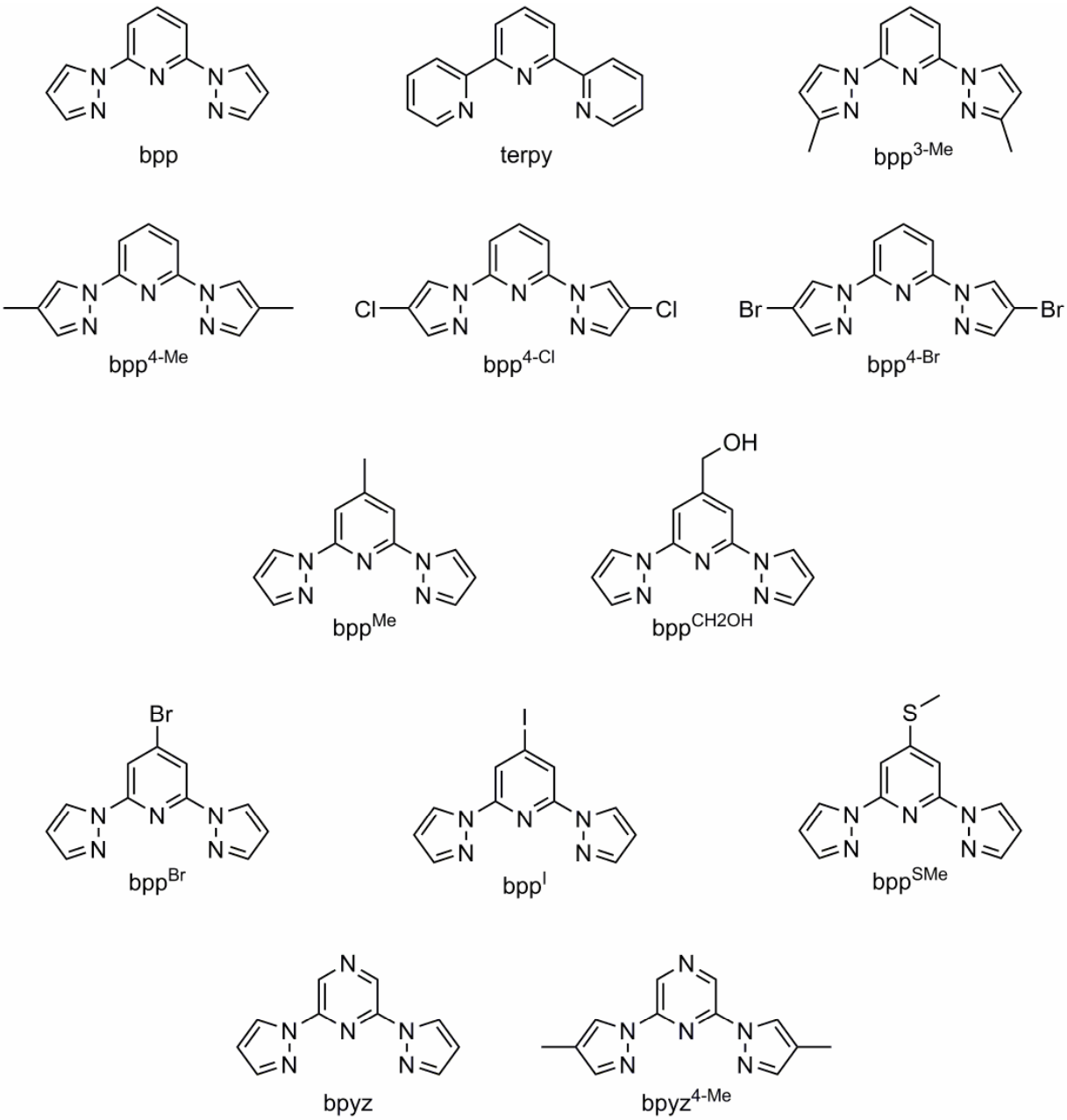

Scheme S3 Ligands referred to in Table S5.

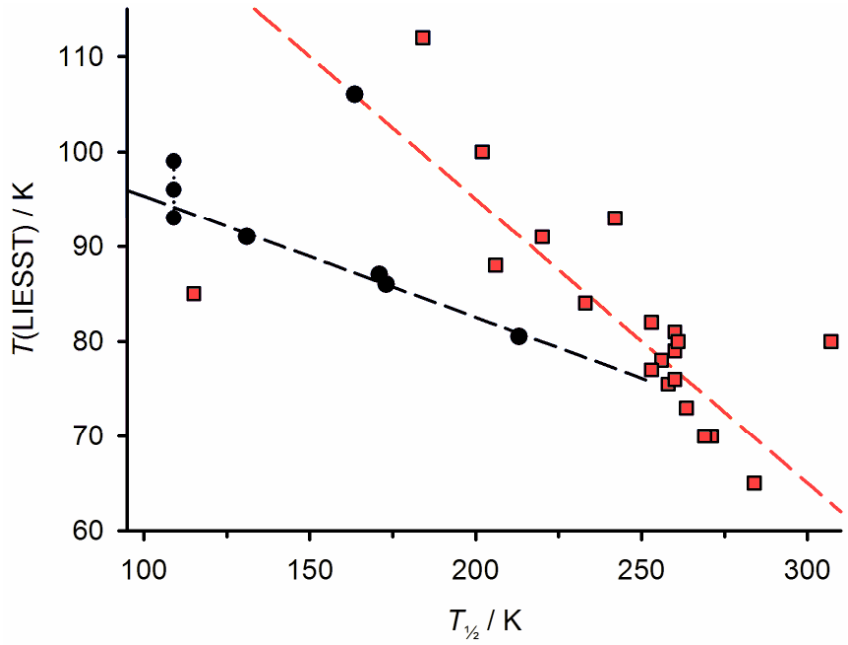

Figure S9 Plot of $T_{½}$ *vs* T(LIESST) for the compounds in this work (black circles), and of previously published compounds from our laboratory (red squares; Table S5). The graph is the same as Fig. 2 in the main article.

The red dashed line shows eq 1 with T_0 = 155 K, close to the T_0 = 150 K correlation that was originally proposed to apply to this family of compounds.[13,15]

$$T(\text{LIESST}) = T_0 - 0.3T_{½} \quad (1)$$

The black dashed line is the best fit linear regression to the new compounds in this study (eq 2), excluding **1[BF$_4$]$_2$**·MeCN. The fitted parameters are T_0 = 108 K anpd a = 0.13.

$$T(\text{LIESST}) = T_0 - aT_{½} \quad (2)$$

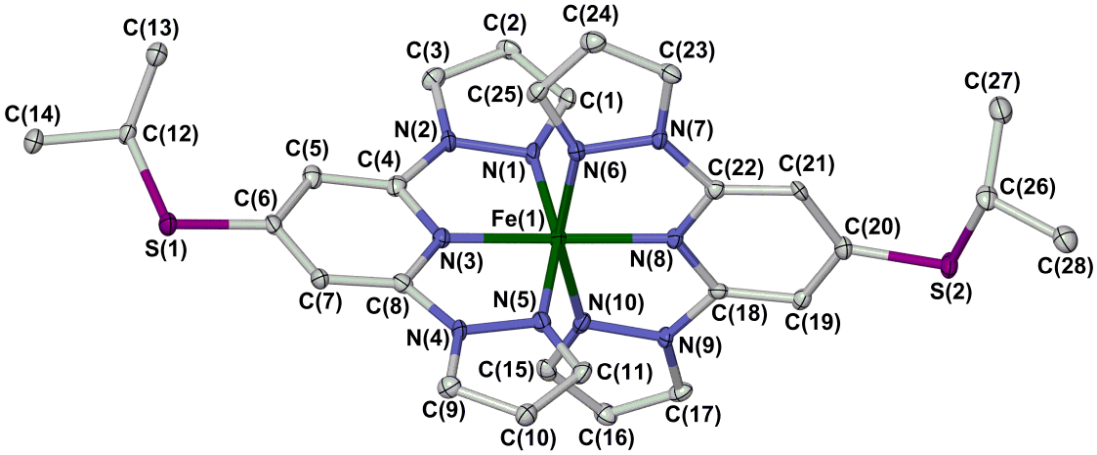

Figure S10. View of the low-spin [FeL_2]$^{2+}$ cation in **1[BF$_4$]$_2$**·H$_2$O at 20 K, showing the atom numbering scheme employed in Table S5. Displacement ellipsoids are at the 50 % probability level, and H atoms have been omitted for clarity. Colour code: C, white; Fe, green; N, blue; S, purple.

Table S6 Selected bond distances and angular parameters for three **1[BF$_4$]$_2$**·solv crystals, under irradiation or thermal trapping (Å, °). See Fig. S10 for the atom numbering scheme. Selected data at higher temperatures from ref. 2 are also included, for comparison.

Σ and Φ are indices characteristic for the spin state of the complex,[6,7] while φ and θ are measures of the deviation of the complex molecule from idealised D_{2d} symmetry (see above).[8,9] Typical values of these parameters for complexes related to [FeL_2]$^{2+}$ are given in ref. 8.

1[BF$_4$]$_2$·MeNO$_2$						
T / K	100(2), Phase 1	15(2), Phase 2			15(2), Phase 3	
	Low-spin	Low-spin			High-spin	
		Molecule A	Molecule B	Molecule C	Molecule A	Molecule B
Fe(1)–N(1)	1.958(3)	1.978(3)	1.977(3)	1.970(3)	2.210(4)	2.215(4)
Fe(1)–N(3)	1.895(3)	1.905(2)	1.896(2)	1.901(2)	2.126(4)	2.132(4)
Fe(1)–N(5)	1.978(3)	1.986(3)	1.959(3)	1.982(3)	2.167(4)	2.166(4)
Fe(1)–N(6)	1.984(3)	1.978(3)	1.982(3)	1.992(3)	2.172(4)	2.158(4)
Fe(1)–N(8)	1.894(3)	1.904(2)	1.903(2)	1.900(3)	2.119(4)	2.118(4)
Fe(1)–N(10)	1.978(3)	1.962(3)	1.986(3)	1.982(3)	2.182(4)	2.166(4)
Σ	90.0(4)	90.0(4)	87.5(4)	87.7(4)	152.4(5)	154.5(5)
Θ	294	294	287	287	466	473
ϕ	174.47(11)	173.69(11)	173.61(12)	176.74(12)	169.97(13)	167.67(14)
θ	87.14	86.72	87.00	87.12	89.19	86.32

1[BF$_4$]$_2$·H$_2$O				
T / K	250(2), Phase 1	150(2), Phase 1	20(2), Phase 1	20(2), Phase 1
	High-spin[a]	Low-spin[a]	Low-spin	High-spin
Fe(1)–N(1)	2.155(3)	1.981(2)	1.976(3)	2.154(2)
Fe(1)–N(3)	2.119(3)	1.8978(19)	1.894(3)	2.123(2)
Fe(1)–N(5)	2.205(3)	1.978(2)	1.975(3)	2.202(2)
Fe(1)–N(6)	2.168(3)	1.964(2)	1.957(3)	2.175(2)
Fe(1)–N(8)	2.100(3)	1.9000(19)	1.893(3)	2.098(2)
Fe(1)–N(10)	2.182(3)	1.986(2)	1.984(3)	2.190(2)
Σ	148.4(4)	88.0(3)	88.3(4)	151.1(3)
Θ	464	288	286	466
ϕ	168.62(12)	175.70(9)	175.72(11)	169.02(8)
θ	86.61(3)	89.15(2)	89.69	89.79

1[BF$_4$]$_2$·MeCN					
T / K	165(2), Phase 1	160(2), Phase 1	85(2), Phase 1	85(2), Phase 1	15(2), Phase 1
	High-spin[a]	Low-spin[a]	Low-spin	High-spin	High-spin
Fe(1)–N(1)	2.174(2)	1.9865(18)	1.9845(15)	2.1745(17)	2.197(3)
Fe(1)–N(3)	2.130(2)	1.9022(16)	1.8987(14)	2.1289(16)	2.122(3)
Fe(1)–N(5)	2.206(2)	1.9717(18)	1.9673(15)	2.2073(17)	2.169(3)
Fe(1)–N(6)	2.169(2)	1.9744(18)	1.9706(15)	2.1721(17)	2.171(3)
Fe(1)–N(8)	2.121(2)	1.9034(16)	1.8986(14)	2.1246(16)	2.117(2)
Fe(1)–N(10)	2.170(2)	1.9664(18)	1.9619(15)	2.1726(17)	2.166(2)
Σ	153.0(3)	88.6(2)	87.7(2)	153.5(2)	152.1(3)
Θ	475	288	287	477	473
ϕ	167.85(8)	174.33(7)	174.26(6)	167.76(6)	168.15(9)
θ	87.84(2)	88.76(2)	89.48	88.31	88.75

[a]Data taken from ref. 2.

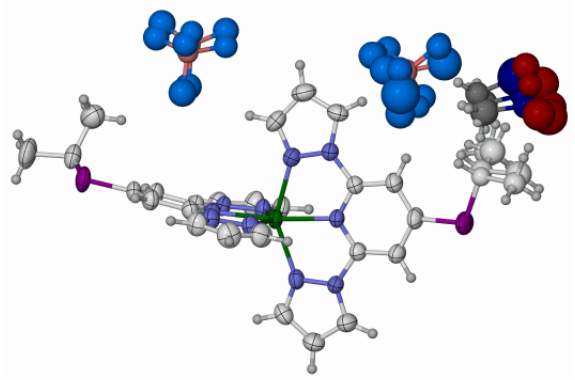

T = 250 K, phase 1, high-spin[2]

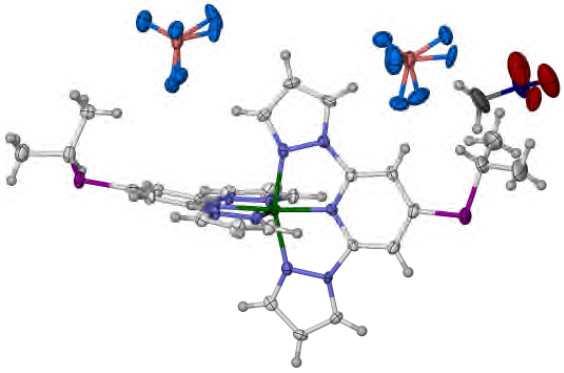

T = 100 K, phase 1, low-spin

molecule A

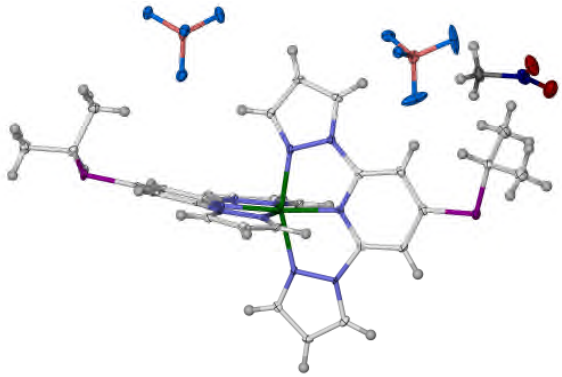

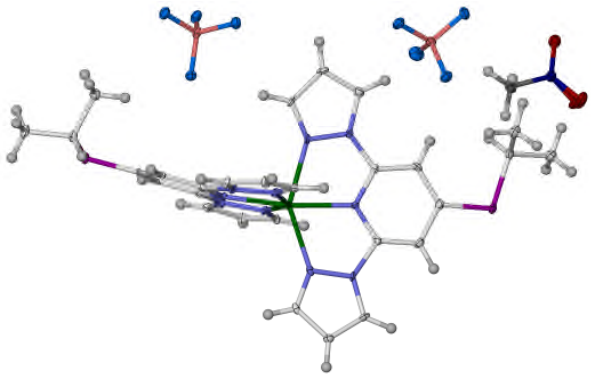

molecule B

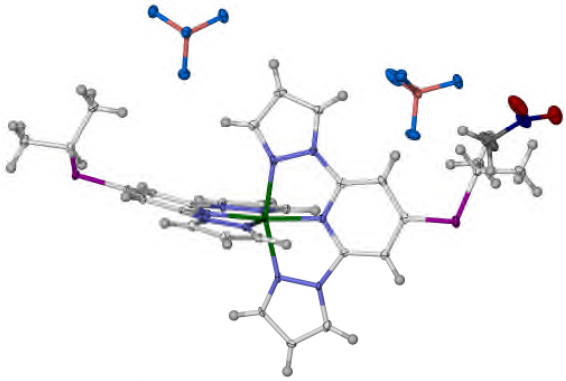

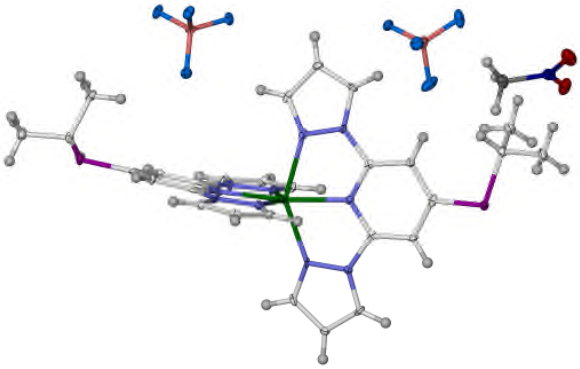

molecule C

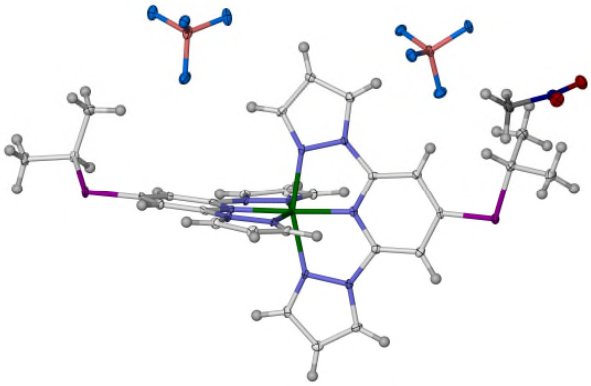

T = 20 K after irradiation, high-spin

T = 20 K, low-spin

Figure S11 Comparison of the disorder in the asymmetric unit of **1[BF$_4$]$_2$**·MeNO$_2$, at different temperatures and following irradiation. Each formula unit in phases 2 and 3 is plotted in the same orientation, to aid comparison. Atomic displacement ellipsoids are drawn at the 50 % probability level.

Colour code: C{complex}, white; C{solvent}, dark gray; H, pale gray; B, pink; F, cyan; Fe, green; N{complex}, pale blue; N{solvent}, dark blue; O, red; S, purple.

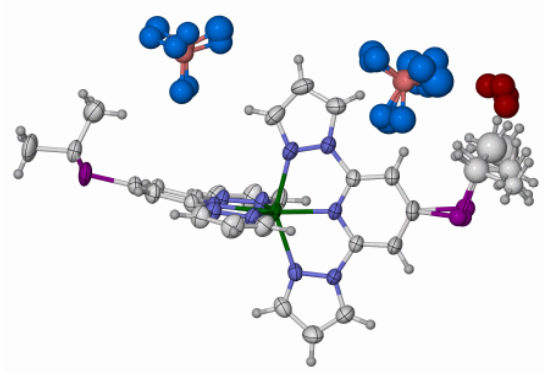

T = 250 K, predominantly high-spin[2]

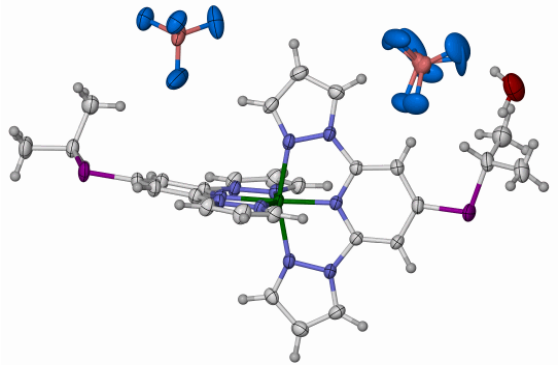

T = 100 K, low-spin[2]

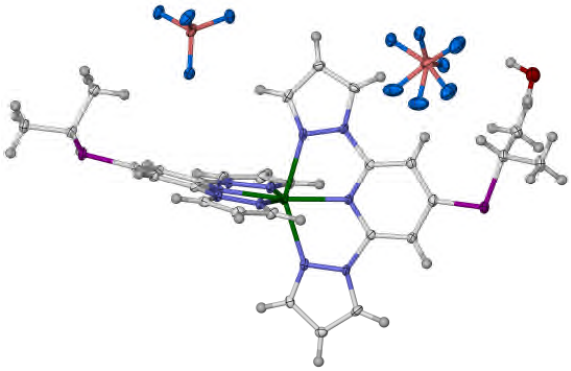

T = 20 K after irradiation, high-spin

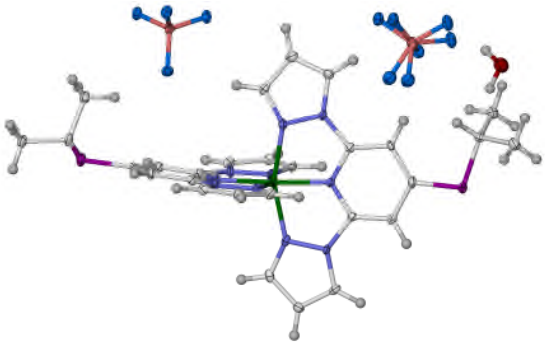

T = 20 K, low-spin

Figure S12 Comparison of the disorder in the asymmetric unit of **1[BF_4]$_2$**·H_2O in phase 1, at different temperatures and following irradiation. Atomic displacement ellipsoids are drawn at the 50 % probability level.

Colour code: C{complex}, white; C{solvent}, dark gray; H, pale gray; B, pink; F, cyan; Fe, green; N{complex}, pale blue; N{solvent}, dark blue; O, red; S, purple.

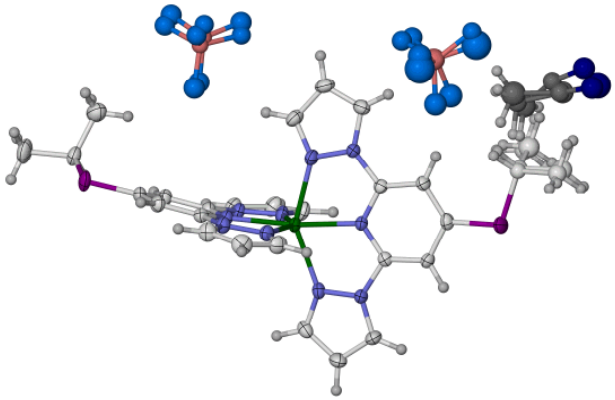

T = 165 K, high-spin[2]

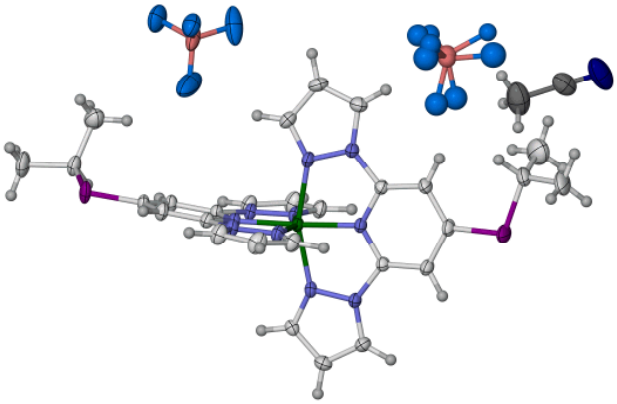

T = 160 K, low-spin[2]

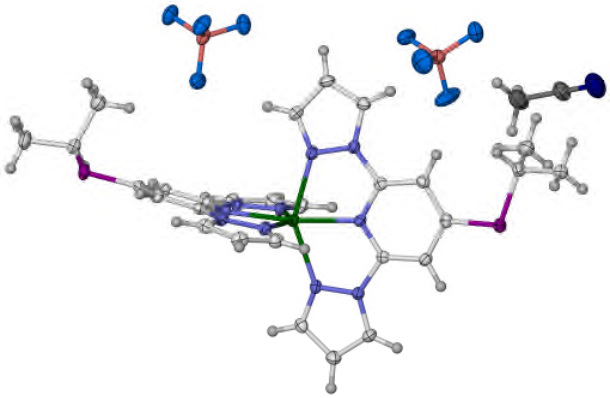

T = 85 K after irradiation, high-spin

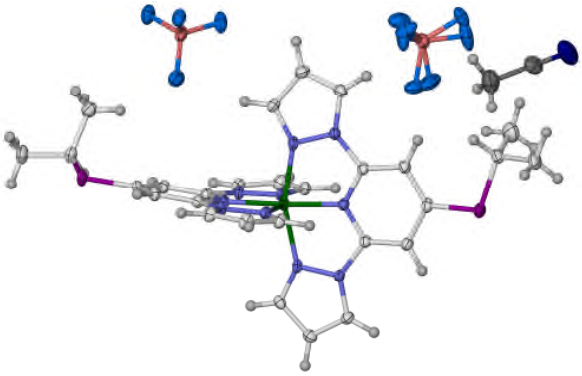

T = 85 K, low-spin

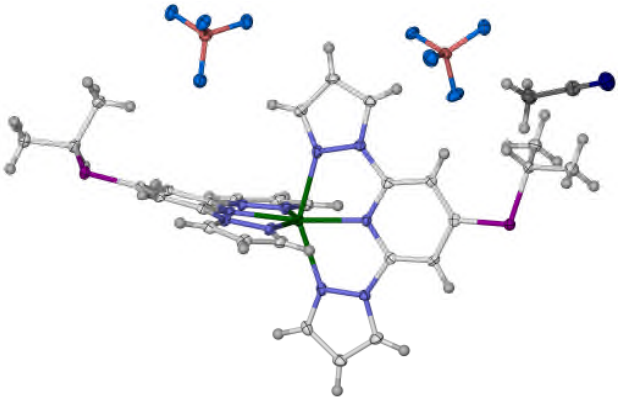

T = 15 K, high-spin

Figure S13 Comparison of the disorder in the asymmetric unit of **1[BF$_4$]$_2$**·MeCN in phase 1, at different temperatures and following irradiation. Atomic displacement ellipsoids are drawn at the 50 % probability level.

Colour code: C{complex}, white; C{solvent}, dark gray; H, pale gray; B, pink; F, cyan; Fe, green; N{complex}, pale blue; N{solvent}, dark blue; S, purple.

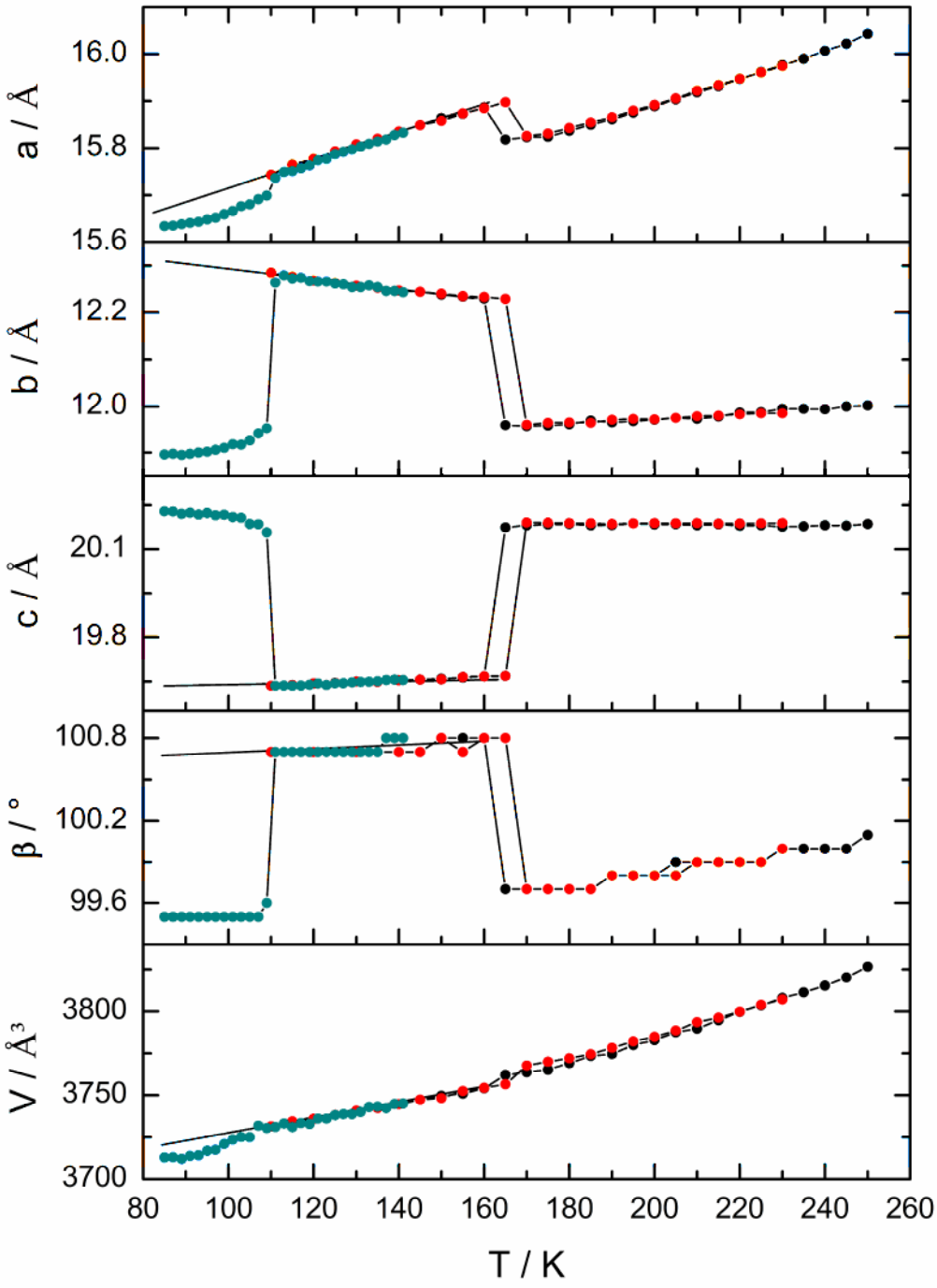

Figure S14 Temperature dependence of the unit cell parameters of **1[BF$_4$]$_2$**·MeCN upon cooling (black) and warming (red) across its thermal SCO transition ($T_{½}$ = 164 K); and, upon warming after irradiation at 660 nm at 85 K (cyan).

The negligible change in unit cell volume during the hysteretic thermal spin transition is consistent with our previous report.[2] The small negative volume expansion after isothermal low→high-spin photoconversion is a rare observation.[22,23]

References

1 C. J. O'Connor, *Prog. Inorg. Chem.*, 1982, **29**, 203.

2 L. J. Kershaw Cook, R. Kulmaczewski, O. Cespedes and M. A. Halcrow, *Chem. Eur. J.*, 2016, **22**, 1789.

3 A. L. Spek, *J. Appl. Cryst.*, 2003, **36**, 7.

4 G. M. Sheldrick, *Acta Crystallogr. Sect. C*, 2015, **71**, 3.

5 L. J. Barbour, *J. Supramol. Chem.*, 2001, **1**, 189.

6 J. K. McCusker, A. L. Rheingold and D. N. Hendrickson, *Inorg. Chem.* **1996**, *35*, 2100.

7 P. Guionneau, M. Marchivie, G. Bravic, J.-F. Létard and D. Chasseau, *Top. Curr. Chem.*, 2004, **234**, 97.

8 M. A. Halcrow, *Coord. Chem. Rev.*, 2009, **253**, 2493.

9 J. M. Holland, J. A. McAllister, C. A. Kilner, M. Thornton-Pett, A. J. Bridgeman and M. A. Halcrow, *J. Chem. Soc. Dalton Trans.*, 2002, 548.

10 S. Vela, J. J. Novoa and J. Ribas-Arino, *Phys. Chem. Chem. Phys.*, 2014, **16**, 27012.

11 L. J. Kershaw Cook, F. L. Thorp-Greenwood, T. P. Comyn, O. Cespedes, G. Chastanet and M. A. Halcrow, *Inorg. Chem.*, 2015, **54**, 6319.

12 a) J.-F. Létard, P. Guionneau, L. Rabardel, J. A. K. Howard, A. E. Goeta, D. Chasseau and O. Kahn, *Inorg. Chem.*, 1998, **37**, 4432;

b) J.-F. Létard, P. Guionneau, O. Nguyen, J. S. Costa, S. Marcen, G. Chastanet, M. Marchivie and L. Capes, *Chem. Eur. J.*, 2005, **11**, 4582.

13 J.-F. Létard, *J. Mater. Chem.*, 2006, **16**, 2550.

14 Other *T*(LIESST) measurements on $[Fe(bpp)_2]X_2$ derivatives:
a) M. Nihei, H. Tahira, N. Takahashi, Y. Otake, Y. Yamamura, K. Saito and H. Oshio, *J. Am. Chem. Soc.*, 2010, **132**, 3553;
b) I. Šalitroš, Olaf Fuhr, R. Kruk, J. Pavlik, L. Pogány, B. Schäfer, M. Tatarko, R. Boča, W. Linert and M. Ruben, *Eur. J. Inorg. Chem.*, 2013, 1049;
c) A. Abhervé, M. Clemente-León, E. Coronado, C. J. Gómez-García and M. López-Jordà, *Dalton Trans.*, 2014, **43**, 9406;
d) I. Šalitroš, L. Pogány, M. Ruben, R. Boča and W. Linert, *Dalton Trans.*, 2014, **43**, 16584;
e) N. Bridonneau, L. Rigamonti, G. Poneti, D. Pinkowicz, A. Forni and A. Cornia, *Dalton Trans.*, 2017, **46**, 4075;
f) K. S. Kumar, I. Šalitroš, E. Moreno-Pineda and M. Ruben, *Dalton Trans.*, 2017, **46**, 9765.

15 C. Carbonera, J. S. Costa, V. A. Money, J. Elhaïk, J. A. K. Howard, M. A. Halcrow and J.-F. Létard, *Dalton Trans.*, 2006, 3058.

16 G. Chastanet, C. A. Tovee, G. Hyett, M. A. Halcrow and J.-F. Létard, *Dalton Trans.*, 2012, **41**, 4896.

17 V. A. Money, C. Carbonera, J. Elhaïk, M. A. Halcrow, J. A. K. Howard and J.-F. Létard, *Chem. Eur. J.*, 2007, **13**, 5503.

18 R. Pritchard, H. Lazar, S. A. Barrett, C. A. Kilner, S. Asthana, C. Carbonera, J.-F. Létard and M. A. Halcrow, *Dalton Trans.*, 2009, 6656.

19 L. J. Kershaw Cook, H. J. Shepherd, T. P. Comyn, C. Baldé, O. Cespedes, G. Chastanet and M. A. Halcrow, *Chem. Eur. J.*, 2015, **21**, 4805.

20 R. Mohammed, G. Chastanet, F. Tuna, T. L. Malkin, S. A. Barrett, C. A. Kilner, J.-F. Létard and M. A. Halcrow, *Eur. J. Inorg. Chem.*, 2013, 819.

21 The following compound undergoes a contraction in its (normalised) unit cell volume during low-spin→high-spin photoconversion, as part of a symmetry-breaking phase transition:
P. Chakraborty, S. Pillet, E. Bendeif, C. Enachescu, R. Bronisz and A. Hauser, *Chem. Eur. J.*, 2013, **19**, 11418.

22 These compounds all undergo the more usual unit cell volume expansion during low-spin→high-spin photoconversion:

a) J. Kusz, H. Spiering and P. Gütlich, *J. Appl. Cryst.*, 2000, **33**, 201;

b) J. Kusz, H. Spiering and P. Gütlich, *J. Appl. Cryst.*, 2001, **34**, 229;

c) M. Marchivie, P. Guionneau, J. A. K. Howard, G. Chastanet, J.-F. Létard, A. E. Goeta and D. Chasseau, *J. Am. Chem. Soc.*, 2002, **124**, 194;

d) E. J. MacLean, C. M. McGrath, C. J. O'Connor, C. Sangregorio, J. M. W. Seddon, E. Sinn, F. E. Sowrey, S. J. Teat, A. E. Terry, G. B. M. Vaughan and N. A. Young, *Chem. Eur. J.*, 2003, **9**, 5314;

e) A. L. Thompson, A. E. Goeta, J. A. Real, A. Galet and M. C. Muñoz, *Chem. Commun.*, 2004, 1390;

f) L. Guérin, N. Huby, E. Collet, L. Toupet, H. Cailleau and K. Tanaka, *J. Phys.: Conf. Ser.*, 2005, **21**, 136;

g) E. Trzop, M. Buron-Le Cointe, H. Cailleau, L. Toupet, G. Molnar, A. Bousseksou, A. B. Gaspar, J. A. Real and E. Collet, *J. Appl. Cryst.*, **2007**, **40**, 158;

h) C.-H. Shih, C.-F. Sheu, K. Kato, K. Sugimoto, J. Kim, Y. Wang and M. Takata, *Dalton Trans.*, 2010, **39**, 9794;

i) E. Collet, M. Lorenc, M. Cammarata, L. Guérin, M. Servol, A. Tissot, M.-L. Boillot, H. Cailleau and M. Buron-Le Cointe, *Chem. Eur. J.*, 2012, **18**, 2051;

j) J.-F. Létard, S. Asthana, H. J. Shepherd, P. Guionneau, A. E. Goeta, N. Suemura, R. Ishikawa and S. Kaizaki, *Chem. Eur. J.*, 2012, **18**, 5924;

k) S. Pillet, E. Bendeif, S Bonnet, H. J. Shepherd and P Guionneau, *Phys. Rev. B*, 2012, **86**, 064106;

l) W. Kaszub, M. Buron-Le Cointe, M. Lorenc, M.-L. Boillot, M. Servol, A. Tissot, L. Guérin, H. Cailleau and E. Collet, *Eur. J. Inorg. Chem.*, 2013, 992;

m) A. Tissot, E. Rivière, R. Guillot, L. Toupet, E. Collet and M.-L. Boillot, *Dalton Trans.*, 2014, **43**, 1063;

n) E. Collet, L. Henry, L. Piñeiro-López, L. Toupet and J. A. Real, *Curr. Inorg. Chem.*, 2016, **6**, 61;

o) E. Milin, V. Patinec, S. Triki, E. Bendeif, S. Pillet, M. Marchivie, G. Chastanet and K. Boukheddaden, *Inorg. Chem.*, 2016, **55**, 11652;

p) D. Zhang, E. Trzop, F. J. Valverde-Muñoz, L. Piñeiro-López, M. C. Muñoz, E. Collet and J. A. Real, *Cryst. Growth Des.*, 2017, **17**, 2736.